LATTE: Open-source, high-performance acoustic and elastic traveltime computation, tomography, and source location

Kai Gao[*,1] and Ting Chen[1]

[1]Earth and Environmental Sciences Division, Los Alamos National Laboratory, Los Alamos, NM 87545, USA

This is a non-peer-reviewed preprint submitted to *EarthArXiv* for public posting. The manuscript has been submitted to *Geophysical Journal International* for peer review. Its structure and content may change with the peer-review process.

*Corresponding author; Email: kaigao@lanl.gov

Abstract

Traveltime-based tomography and source location are classical but important approaches to revealing subsurface structures and understanding spatiotemporal distribution of seismicity ranging from local to global scales. We develop an open-source, high-performance implementation of eikonal equation solving and adjoint-state theory to perform traveltime computation, velocity tomography, and source location in 2D/3D acoustic and elastic media. Specially, we develop novel regularization schemes based on total generalized p-variation, structural similarity, and multitask machine learning models to improve the fidelity and interpretability of inverted model and source parameters. Additionally, our implementation encloses several notable features: its exploits both absolute-difference or double-difference misfit of traveltime to achieve high-fidelity velocity tomography, source location, and source origin time estimation; it enables flexible traveltime computation, tomography, and location in both 2D/3D acoustic and elastic media by allowing arbitrary source and receiver distribution; and we develop a perturbation-based optimal step size computation method to reduce the computational cost. Leveraging both shared-memory and distributed memory parallel programming models, our implementation provides a highly efficient framework for traveltime-based computation, tomography, and source location. We demonstrate the efficacy and efficiency of our method and implementation through several synthetic data examples.

1 Introduction

Traveltime-based tomography and source location are classical but also important approaches to revealing subsurface structures and understanding seismicity ranging from local scale to global scales. In an era of full-waveform-based imaging and inversion, traveltime-based methods still hold their advantage especially in terms of computational efficiency in different applications.

Traveltime computation is the foundation for traveltime-based subsurface characterization. Early works of traveltime computation were mostly based on ray tracing by solving an one-point initial value problem or two-point boundary value problem (Pereyra et al., 1980; Grechka and McMechan, 1996; Sadeghi et al., 1999; Meléndez et al., 2015). While ray-based methods are efficient for sparse source-receiver geometry, the computational complexity is directly proportional to the number of source-receiver pairs as well as the complexity of velocity model in an inversion. Wavefront construction methods (Vinje et al., 1993; Lambaré et al., 1996; Gibson et al., 2005; Chambers and Kendall, 2008) compute traveltime and amplitude by approximating wavefronts and interpolating new rays on-the-fly, but is also more computationally demanding compared with conventional ray-based approaches. Vidale (1988) developed the first eikonal-equation-based approach to computing first-arrival traveltime. Later developments based on the eikonal equation include expanding wavefront methods (Podvin and Lecomte, 1991; Qin et al., 1992), fast marching methods (Sethian and Popovici, 1999; Rawlinson and Sambridge, 2004; Zhang et al., 2006), fast sweeping methods (Tsai et al., 2003; Zhao, 2004; Kao et al., 2004, 2005; Fomel et al., 2009; Luo and Qian, 2011; Waheed et al., 2015b), etc. Recent developments of eikonal solving also include solvers on triangular or unstructured mesh (e.g., Qian et al., 2007; Le Bouteiller et al., 2019), high-order and non-oscillatory solvers (e.g., Kim and Cook, 1999; Kim, 2002; Zhang et al., 2006; Luo and Qian, 2011; Luo et al., 2012), solvers for anisotropic media (Qian and Symes, 2002; Wang et al., 2006; Waheed et al., 2015a; Waheed and Alkhalifah, 2017), and so on. To solve the source singularity issue, one of the major problems intrinsic to eikonal solving, Fomel et al. (2009) and a number of subsequent works (e.g., Luo and Qian, 2011, 2012; Luo et al., 2012) decompose traveltime field through addition or multiplication and achieve accurate traveltime computation for near-source region and correspondingly higher accuracy in the far-field region.

Traveltime tomography is a classical inversion method to estimate subsurface medium properties using traveltime information of seismic signals (e.g., Wu and Toksöz, 1987; Schuster and Quintus-Bosz, 1993; Zelt and Barton, 1998; Zhang and Toksöz, 1998). In contrast to more recent full-waveform inversion (FWI) (e.g. Tarantola, 1984; Mora, 1987; Virieux and Operto, 2009) that uses both traveltime and the amplitude information for estimating medium parameters, traveltime tomography uses only traveltime information, therefore leads to more convex objective function but usually lower-resolution results. In addition, traveltime-based tomography usually enjoys a sheer advantage of low computational cost compared with full-waveform methods, which require solving full wave equations. Early traveltime tomography methods rely on seismic rays, and the model update concentrates merely on ray paths. Studies show that it is also important to consider the band-limited ray path effect and update the model parameters that are near the ray paths, or even use the "full" traveltime information inherited in full seismic wavefields (e.g., Michelena and Harris, 1991; Woodward, 1992; Yomogida, 1992; Schuster and Quintus-Bosz, 1993; Vasco et al., 1995; Snieder and Lomax, 1996; Marquering et al., 1999; Spetzler and Snieder, 2004; Pyun et al., 2005; Xu et al., 2006; Liu et al., 2009; Luo et al., 2016; Zelt and Chen, 2016). These approaches take the finite-frequency effect into consideration, and lead to more accurate tomography results compared with classical ray tomography, but usually require higher computational costs (Luo and Schuster, 1991; Michelena and Harris, 1991; Woodward, 1992; Schuster and Quintus-Bosz, 1993; Vasco et al., 1995; Liu et al., 2009; Luo et al., 2016).

Ray-based traveltime tomography is usually formulated in a large linear system and is solved using iterative strategies, the computational cost of which is directly proportional to the number of source-receiver pairs and the number of model parameters. For active-source applications, the number of source-receiver pairs can be prohibitively large, therefore can result in high computational cost. In addition, as ray computation can fail in complex heterogeneous media (e.g., Rawlinson et al., 2010), ray-based traveltime tomography may suffer from applicability and accuracy issue in complex geological models. In observation of these issues, traveltime tomography was formulated in a nonlinear inversion framework using the adjoint-state method (Sei and Symes, 1994; Leung and Qian, 2006; Taillandier et al., 2009; Huang and Bellefleur, 2012), which was previously applied to computing FWI gradients (Plessix, 2006; Fichtner et al., 2006; Liu and Tromp, 2006). The main advantage of the adjoin-state traveltime tomography is that the problem dimension is independent of the number of source-receiver pairs and is only determined by the number of sources and the dimension of the discretized model. For each common-shot gather, the adjoint-state method only requires solving an eikonal equation and an adjoint-state equation in a similar fashion with FWI gradient computation. Because the traveltime fields in the adjoint-state traveltime methods are computed for the whole space, the kernel in the adjoint-state traveltime naturally approximate the band-limit effect in the sophisticated fat-ray or wave-path approaches (Taillandier et al., 2009; Bretaudeau et al., 2014). In addition, one can use efficient eikonal solvers to obtain the traveltime field and the adjoint-state field, e.g., the fast-sweeping method (Zhao, 2004) with a computational complexity of $\mathcal{O}(N)$, where N is the number of grid points in the discretized model. Traveltime tomography can also use reflection traveltime information (e.g., Zhang et al., 1998; Korenaga et al., 2000; Huang and Bellefleur, 2012; Meléndez et al., 2015; Zhang et al., 2023) for deriving deep subsurface structures when there is no sufficiently wide-aperture traveltime available.

Depending on the complexity of the target model, traveltime tomography may need proper preconditioning and regularization schemes for improving the convergence. Regularized geophysical inversion has a long history (Zhdanov, 2002), of which the Tikhonov regularization is frequently used (Tikhonov et al., 1995; Asnaashari et al., 2013). Rudin et al. (1992) developed the methodology of the total variation (TV) to reconstruct sharp edges of images in the context of image analysis and processing. Anagaw (2011) applied this method to geophysical inverse problems to promote sharp interfaces of models. In the context of FWI, Guitton (2012) developed a blocky regularization scheme to promote interface reconstruction. Lin and Huang (2014) developed a modified TV (MTV) regularization scheme to obtain clean and accurate TV regularization results with the split-Bregman technique (Goldstein and Osher, 2009). Lin et al. (2015) applied this regularization to double-difference traveltime tomography (Zhang and Thurber, 2003). Esser et al. (2016) developed an asymmetric TV regularized FWI, in which they penalizes the model discontinuities only in the vertical direction in an asymmetric way, resulting in high-quality reconstruction of deep regions and large medium parameter contrasts. Gao and Huang (2019) developed a total generalized p-variation regularization scheme that preserves both sharp interfaces and piecewise smooth medium property variations. In the context of ground-penetrating radar imaging, Gao et al. (2022) developed a machine-learning (ML) based regularizer to improve the resolution, structure coherence, and fault delineation.

Source location has been one of the most classical problems in seismology. Accurately locating seismic event to their correct spatiotemporal locations is the key to understand the evolution of earthquakes and their correlation with faults. Geiger's method has been the classical principle of source location, which computes the source location through the partial derivatives with respect to location in a framework of linear traveltime equation based on Taylor series expansion. Initially formulated within the framework of ray method (Thurber, 1983), the principle was later applied in the context of wave equation and eikonal equation (Tong et al., 2016; Tong, 2021a) for determining source location. In a departure from Geiger's location method, Waldhauser and Ellsworth (2000) leveraged the similarity between the ray paths of two close events, and attributed the time difference of two events observed at a same station to the spatial separation of the two events through the so-called double difference (DD). The method exploits both absolute traveltime and differential time, and provides an effective way to remove the receiver-side structure uncertainties and obtain high-resolution source location. The principle was later applied to joint velocity tomography and source location (Zhang and Thurber, 2003, 2006) in the framework of seismic rays. The methodology of DD, along with the open-source implementation (hypoDD and tomoDD), gained a wide variety of applications ranging from earthquake seismology (e.g., Guo and Thurber, 2021; Zeng et al., 2016) to CO_2 reservoir microseismicity monitoring (Dando et al., 2021), to list a few. Yuan et al. (2016) applied DD to FWI. Tong et al. (2024) extended the methodology of DD or differential traveltime to adjoint-state traveltime tomography and hypocenter location, allowing for complex velocity models.

In this work, we develop an open-source, high-performance implementation of traveltime computation, tomography, and source location. Specially, we develop novel regularization schemes for updating model and source parameters, aiming to improve the fidelity and interpretability of inversion results. The motivation for us to develop this work is two-fold.

Firstly, current traveltime-based tomography and source location method do not present a systematic approach to regularizing model and source parameters. The damping strategy used by tomoDD (Zhang and Thurber, 2003, 2006) is for stabilizing the inversion by resolving the imbalance between ray path density and grid spacing, but does not primarily regularize model parameters. The MTV regularization developed by Lin et al. (2015) is a more modern approach to model parameter regularization, yet the work is developed in the framework of ray-based tomoDD. As to the source parameter, we are unaware of any systematic method that regularizes source locations. For both global to regional-scale earthquakes and local-scale microseismicity applications, the fundamental observation is that seismicity is strongly correlated with faults or fractures, which is consistent with well-established seismic moment source theory (Aki and Richards, 2002). In response to these two issues, in this work, we develop a novel regularization scheme to model parameter update (for both first-arrival traveltime tomography and joint tomography-location). The new regularization scheme consists of a total generalized p-variation (TGpV) regularizer and a P-S wave velocity structure similarity regularizer. The first regularizer results in piecewise smooth updated velocity models by penalizing both the first- and second-order total variations (Rudin et al., 1992; Goldstein and Osher, 2009; Knoll et al., 2011; Gao and Huang, 2019), while second regularizer results in structurally consistent v_p and v_s models by imposing v_p/v_s ratio limits and applying median and Gaussian smoothing. Our test results show that such a joint regularizer results in elastic parameter models of higher fidelity. Meanwhile, we develop a novel ML-based source parameter regularizer for improving the spatial consistency between faults/fractures and inverted seismic locations. In specific, we develop a supervised multitask ML model to infer faults from a source image, a supervised multitask ML model to refine the inferred faults, and then use the inferred and refined faults as a "guidance" to guide the update of source locations over iterations. Both regularization schemes lead to better interpretability of inversion results.

Secondly, as of today, there have been numerous open-sources codes for traveltime computation (e.g., de Kool et al., 2006; White et al., 2020; Chen et al., 2023). On the contrary, the available open-source implementation of traveltime-based tomography and source location is limited (Rawlinson et al., 2006; Fang et al., 2019) in addition to hypoDD (Waldhauser and Ellsworth, 2000) and tomoDD (Zhang and Thurber, 2003), with different levels of convenience to use. When considering eikonal-equation and adjoin-state-equation-based traveltime tomography and source location, we know few available open-source, fully-functional codes, except for instance, RAJZEL (Koehn and De Nil, 2022), ATT_Training (Tong, 2021b), both apply only to 2D acoustic media. Our work therefore aims specifically to build an open-source, systematic, high-performance implementation enclosing traveltime computation, first-arrival traveltime tomography, source location, as well as joint tomography-location, based on the eikonal equation (Fomel et al., 2009) and the adjoint-state equation (Leung and Qian, 2006; Taillandier et al., 2009) for both 2D/3D acoustic and elastic media. In addition, we intend to include the novel model and source parameter regularization schemes developed in this paper to this package, thus enhancing its capability in inverting complex models and fault-related source locations. An additional intention is that we aim to provide a hybrid shared- and distributed memory parallel implementation of both factorized eikonal equation and adjoint-state equation, thus, to achieve high computational efficiency for large inversion problems on modern high-performance computing platforms. We also design user-friendly parameter input and result output in our implementation to enable convenient setup for inversions involving complex model, observation geometry, data, and parameter tuning. To distinguish our work with existing works, we name our open-source implementation as LATTE – Los Alamos Travel-Time package based on Eikonal equation.

The rest of the paper is organized as follows. In the Methodology section, we detail the methods and algorithms we use for traveltime computation, first-arrival traveltime tomography (FATT), and source location, and joint tomography-location (TLOC). Specially, we describe the algorithms associated with optimal step size computation in FATT and TLOC based on a small-perturbation approach and detail a TGpV- and $v_p - v_s$ similarity-based model parameter regularization scheme and an ML-based fault-constrained source parameter regularization scheme to improve the fidelity and interpretability of inversion results. In the Numerical Results section, we use five examples to validate the efficacy and accuracy of our methods and implementation. We summarize our work in Conclusions.

2 Methodology

2.1 Traveltime computation

The eikonal equation in isotropic media is an infinitely high-frequency approximation to wave equation:

$$v^2|\nabla t|^2 = 1, \qquad t(\mathbf{x}_s) = 0, \tag{1}$$

where $t = t(\mathbf{x})$ is the traveltime field associated with a velocity model $v = v(\mathbf{x})$ and a source location $\mathbf{x}_s$. When there is a non-zero source initiation time t_0, we add t_0 to $T(\mathbf{x})$ as $T(\mathbf{x}) + t_0$ to obtain its true arrival time.

A known issue associated with solving equation (1) is that the traveltime field curvature at the source location is infinite, resulting in notable inaccuracy near the source location, which can propagate outwards. In our LATTE implementation, we adopt the factorized eikonal equation (Fomel et al., 2009) to mitigate the issue:

$$v^2 \sum_{i=1}^{3} \left(t_0 \frac{\partial \tau}{\partial x_i} + \frac{\partial t_0}{\partial x_i} \tau \right)^2 = 1, \tag{2}$$

$$t(\mathbf{x}) = t_0(\mathbf{x})\tau(\mathbf{x}) + \eta_0, \qquad t_0(\mathbf{x}_s) = 0, \qquad \tau(\mathbf{x}_s) = 1, \tag{3}$$

where x_i with $i = 1, 2, 3$ represent spatial coordinates, $t_0 = t_0(\mathbf{x})$ is a background traveltime field computed by analytical expression for avoid source singularity, $\tau = \tau(\mathbf{x})$ is a multiplicative field, which is also the field to be solved with through equation (2). In addition, η_0 is a scalar value representing the origin time of the source and is added to the computed traveltime field after t is obtained; $\mathbf{x}_s$ represent the source location.

We generalize equation (2) to the scenario of simultaneous multiple point sources, where each source may have a nonzero origin time. Achieving an ensemble source is trivial with non-factorized eikonal equation, but the methodology is not straightforward for factorized eikonal equation. If a source is an ensemble source consisting of multiple single-point sources $\{\mathbf{s}_i\}$, each point with different origin time $\{\eta_0(\mathbf{s}_i)\}$, then the background traveltime field can be computed as

$$t_0(\mathbf{x}) = \min_{i=1,\cdots,M_s} \{t_0(\mathbf{x};\mathbf{s}_i) + \eta_0(\mathbf{s}_i)\}\,, \tag{4}$$

while the initial condition for τ remains the same: $\tau(\mathbf{x};\mathbf{s}_i) = 1$ ($i = 1, 2, \cdots, M_s$), where M_s is the number of single point sources in the ensemble source. Constructing t_0 for an ensemble source requires computing all $t_0(\mathbf{x};\mathbf{s}_i)$ associated with the single-point sources. Therefore, we solve the forward modeling problem using

$$v^2 \sum_{i=1}^{3} \left(t_0 \frac{\partial \tau}{\partial x_i} + \frac{\partial t_0}{\partial x_i} \tau \right)^2 = 1, \tag{5}$$

$$t(\mathbf{x}) = t_0(\mathbf{x})\tau(\mathbf{x}), \qquad t_0(\mathbf{x}) = \min_{i=1,\cdots,M_s} \{t_0(\mathbf{x};\mathbf{s}_i) + \eta_0(\mathbf{s}_i)\}\,, \qquad \tau(\mathbf{x};\mathbf{s}_i) = 1. \tag{6}$$

To simplify notations, we denote equation (5) as a functional:

$$\mathcal{E}(v, t; \mathbf{s}, \eta_0) = \mathcal{E}(v, t; \{\mathbf{s}_i\}, \{\eta_0(\mathbf{s}_i)\}) = 0, \tag{7}$$

where $v = v(\mathbf{x})$ is the P- or S-wave velocity of a medium, and $\{\cdot\}$ represents an ensemble.

In elastic media, we solve two decoupled eikonal equations:

$$\mathcal{E}(v_p, t_p; \mathbf{s}, \eta_0) = 0, \quad \mathcal{E}(v_s, t_s; \mathbf{s}, \eta_0) = 0, \tag{8}$$

where the P- and S-traveltime fields share the same source location and origin time.

For of the purpose of future extensibility, our LATTE also implements seismic reflection traveltime computation, where we assume that a reflector can be represented as an ensemble of points, say, $I = \{\mathbf{x}_1, \mathbf{x}_2, \cdots, \mathbf{x}_l\}$, i.e., a collection of l spatial coordinates. Then we solve the following eikonal equations to obtain the PP reflection (i.e., P incidence to P reflection) traveltime associated with a reflector I^h ($h = 1, 2, \cdots, H$):

$$\mathcal{E}(v_p, t_p; \mathbf{s}, \eta_0) = 0, \quad \mathcal{E}(v_p, t_{pp}^h; I^h, t_p(I^h)) = 0, \tag{9}$$

where the discrete traveltime $t_p(I)$ is the spatially varying origin time associated with the reflector. The equation can be extended to arbitrary number of reflectors, but the incident traveltime field t_p only needs to be computed once. Similarly, we identify the following eikonal equations to obtain PS reflection (i.e., P incidence to S reflection) traveltime in elastic media:

$$\mathcal{E}(v_p, t_p; \mathbf{s}, \eta_0) = 0, \quad \mathcal{E}(v_s, t_{ps}^h; I^h, t_p(I^h)) = 0, \tag{10}$$

where in the second equation, the velocity is v_s rather than v_p. This can be straightforwardly extended to the case of S-wave incidence and SS/SP reflections.

In LATTE, we accelerate the fast sweeping eikonal solving (and the adjoint-state equation solving detailed below) by adopting and slightly modifying the parallel strategy developed by Detrixhe et al. (2013). For completeness, we detail our parallel fast-sweeping algorithms in Appendix A.

2.2 First-arrival traveltime tomography

Adjoint-state first-arrival traveltime tomography (FATT) based on eikonal equation was established by Leung and Qian (2006) and Taillandier et al. (2009). For completeness, we first review the fundamental definitions of FATT. The original FATT is developed based on minimizing L_2-norm absolute-difference (AD) misfit function between the observed and the synthetic first-arrival traveltime (Taillandier et al., 2009), i.e.,

$$\mathcal{J}(v_p) = \frac{1}{2}\sum_{i=1}^{N_s}\sum_{j=1}^{N_r^i}\left[t(v_p, \mathbf{s}_i, \mathbf{r}_j) - T(\mathbf{s}_i, \mathbf{r}_j)\right]^2, \tag{11}$$

where N_s is the number of sources, and N_r^i is the number of receivers associated with the i-th source. AD-FATT is not immune to nonzero source origin time, i.e., if there is a nonzero origin time η_0 associated with T, it must be estimated before AD-FATT.

One can also formulate FATT using double-difference or differential time misfit function (Zhang and Thurber, 2003; Tong et al., 2024)

$$\mathcal{J}(v_p) = \frac{1}{2}\sum_{i=1}^{N_s}\sum_{j=1}^{N_r^i}\sum_{k=1}^{N_r^i}\left[(t_p(v_p, \mathbf{s}_i, \mathbf{r}_j) - t_p(v_p, \mathbf{s}_i, \mathbf{r}_k)) - (T_p(\mathbf{s}_i, \mathbf{r}_j) - T_p(\mathbf{s}_i, \mathbf{r}_k))\right]^2. \tag{12}$$

DD-FATT is immune to nonzero source origin time. Both misfit functions can be used for inverting v_p and v_s. To simplify notations, we use a generalized symbol $\mathcal{D}(t, T; \mathbf{s}, \mathbf{r})$ to represent the misfit associated with a source $\mathbf{s}_i$:

$$\mathcal{D}(t, T; \mathbf{s}_i, \mathbf{r}) = \sum_{j=1}^{N_r^i}\left[t(v, \mathbf{s}_i, \mathbf{r}_j) - T(\mathbf{s}_i, \mathbf{r}_j)\right]^2, \tag{13}$$

$$\mathcal{D}(t, T; \mathbf{s}_i, \mathbf{r}) = \sum_{j=1}^{N_r^i}\sum_{k=1}^{N_r^i}\left[(t(v, \mathbf{s}_i, \mathbf{r}_j) - t(v, \mathbf{s}_i, \mathbf{r}_k)) - (T(\mathbf{s}_i, \mathbf{r}_j) - T(\mathbf{s}_i, \mathbf{r}_k))\right]^2, \tag{14}$$

where v is the velocity associated with t, and a symbol $\Delta(t, T; \mathbf{s}, \mathbf{r})$ to represent the traveltime residual associated with a trace $\mathbf{r}_j$:

$$\Delta(t, T; \mathbf{s}_i, \mathbf{r}_j) = t(v, \mathbf{s}_i, \mathbf{r}_j) - T(\mathbf{s}_i, \mathbf{r}_j), \tag{15}$$

$$\Delta(t, T; \mathbf{s}_i, \mathbf{r}_j) = \sum_{k=1}^{N_r^i} \left[(t(v, \mathbf{s}_i, \mathbf{r}_j) - t(v, \mathbf{s}_i, \mathbf{r}_k)) - (T(\mathbf{s}_i, \mathbf{r}_j) - T(\mathbf{s}_i, \mathbf{r}_k)) \right]. \tag{16}$$

Based on our arguments in Appendix B, for a source $\mathbf{s}_i$, the adjoint-state equation for AD- or DD-FATT reads

$$\nabla \cdot \left[\lambda_p(\mathbf{x}) \nabla t_p(v_p, \mathbf{x}) \right] = \sum_{j=1}^{N_r} \Delta(t_p, T_p, v_p, \mathbf{s}_i, \mathbf{r}_j). \tag{17}$$

The gradient of $\mathcal{J}(v_p)$ with respect to v_p associated with all sources is

$$\frac{\partial \mathcal{J}}{\partial v_p}(\mathbf{x}) = -\sum_{i=1}^{N_s} \frac{\lambda_{p,i}(\mathbf{x})}{v_p^3(\mathbf{x})}, \tag{18}$$

where $\lambda_{p,i}$ represents the adjoint-state variable associated with $\mathbf{s}_i$. The above equations can be straightforwardly extended to elastic case where both P and S-arrival traveltimes are used.

We adopt a ray-density preconditioning scheme to the common-source gradients (Li et al., 2017; Zhang et al., 2023) to improve traveltime field illumination and thus accelerate convergence. Specifically, for each source, in addition to computing the adjoint field λ, we also compute an adjoint energy field λ_e using

$$\nabla \cdot \left[\lambda_e(\mathbf{x}) \nabla t_p(v_p, \mathbf{x}) \right] = \sum_{j=1}^{N_r} C(\mathbf{r}_j), \tag{19}$$

where $C(\mathbf{r}_j) = 1$, and compute the gradient as

$$\frac{\partial \mathcal{J}}{\partial v_p}(\mathbf{x}) = -\sum_{i=1}^{N_s} \frac{\lambda_{p,i}(\mathbf{x})}{\lambda_e + \epsilon \max(|\lambda_e|)}, \tag{20}$$

where we choose $\epsilon = 10^{-3} \sim 10^{-4}$ to avoid division of zero.

We implement three types of nonlinear inversion schemes in LATTE to perform FATT: steepest decent (SD), nonlinear conjugate gradient (NCG), and limited-memory Broyden-Fletcher-Goldfarb-Shanno (*l*-BFGS) schemes. The three schemes differ in the way of computing the search direction based on the gradient. Detailed algorithms can be found in Nocedal and Wright (2006).

All the three schemes require determination of an optimal step size at each iteration for properly updating the velocity model. In linear search or quadratic search method, an optimal step size is computed based on finding the root of quadratic equation. In such a case, usually the minimal number of forward modeling to determine the optimal step size is $M \geq 3$. Inspired by an early work for FWI (Gauthier et al., 1986), here we develop a perturbation-based method to compute the optimal step size. Specifically, at each FATT iteration l, after obtaining the search direction $\Delta m^{(l)}$, we compute the optimal step size as

$$\alpha_m^{(l)} = \frac{\sum_{i=1}^{N_s} |\beta_i| \cdot |\gamma_i|}{\sum_{i=1}^{N_s} \|\beta_i\|^2}. \tag{21}$$

The time residual vectors are

$$\beta_{i,j}(m) = \Delta\left(t(m^{(l-1)} + \epsilon\Delta m^{(l)}), t(m^{(l-1)}); \mathbf{s}_i, \mathbf{r}_j\right), \tag{22}$$

$$\gamma_{i,j}(m) = \Delta\left(T, t(m^{(l-1)}); \mathbf{s}_i, \mathbf{r}_j\right), \tag{23}$$

where the small perturbation trial coefficient $\epsilon = 0.05$, or equals to a small value that ensures $m_{\min} \leq m^{(l-1)} + \epsilon\Delta m^{(l)} \leq m_{\max}$, where $m_{\min}$ and $m_{\max}$ are box bounding limits set as hyper-parameters for the inversion, if necessary. In the above equations, Δm represents the search direction computed using steepest decent, NCG, or l-BFGS. Therefore, at each iteration, in addition to solving the eikonal equation once and the adjoint-state equation once, we only need to solve the eikonal equation for one additional time based on the perturbed model $m^{(l-1)} + \epsilon\Delta m^{(l)}$ for determining $\alpha_m^{(l)}$. After that, the updated model in the l-th FATT iteration is

$$m^{(l)} = m^{(l-1)} + \alpha_m^{(l)} \Delta m^{(l)}. \tag{24}$$

Our strategy effectively reduces the total computational complexity of each tomography iteration from $\mathcal{O}((M+2)N_s)$ where $M \geq 3$ to $\mathcal{O}(3N_s)$. It is worth noting that in some cases, the number of required forward modeling can be $M > 1$, especially when the valley of loss is narrow and a large step may cause "overshoot," i.e., the resulting step size causes the misfit in the l-th iteration (this iteration) to be higher than that at the $(l-1)$-th iteration (previous iteration). In this case, given an initial step size $\alpha_m^{(l)}$ computed from the perturbation-bases strategy, we reduce the step size by half every time, and check if the resulting misfit is smaller than that of the last iteration. When it is smaller than the misfit of the last iteration, we then choose the reduced $\alpha_m^{(l)}$ as the optimal step size for this iteration. At early iterations, this check is almost not necessary as a search direction can always reduce the misfit. However, at later iterations where the inversion reaches a local minimum, such a trial-and-error may become necessary, making the number of additional forward modeling $M > 1$.

For elastic FATT, we compute the optimal step size in the l-th iteration as

$$\alpha^{(l)} = \frac{\sum_{i=1}^{N_s} \left(|\beta_i(v_p)| \cdot |\gamma_i(v_p)| + |\beta_i(v_s)| \cdot |\gamma_i(v_s)|\right)}{\sum_{i=1}^{N_s} \left(\|\beta_i(v_p)\|^2 + \|\beta_i(v_s)\|^2\right)}, \tag{25}$$

and update v_p and v_s using this step size:

$$v_p^{(l)} = v_p^{(l-1)} + \alpha^{(l)} \Delta v_p^{(l)}, \tag{26}$$

$$v_s^{(l)} = v_s^{(l-1)} + \alpha^{(l)} \Delta v_s^{(l)}. \tag{27}$$

Note that the optimal step size computed with equation (25) is more like an "averaged" or "balanced" optimal step size rather than a direct extension from equation (21) for multi-component traveltime data, which can avoid unstable results for unbalanced data misfit during inversion.

2.3 Joint first-arrival traveltime tomography and source location

Our LATTE contains a functionality, TLOC, to perform joint tomography, hypocenter location, and origin time inversion. The same functionality can also perform DD-based simultaneous tomography and hypocenter location, mitigating the need of estimating an origin time for each source.

The misfit function for joint tomography-location in elastic media reads

$$\mathcal{J}(v_p, v_s, \mathbf{s}, \eta_0) = \frac{1}{2} \sum_{i=1}^{N_s} \left[\mathcal{D}(t_p + \eta_0(\mathbf{s}_i), T_p; \mathbf{s}_i, \mathbf{r}) + \mathcal{D}(t_s + \eta_0(\mathbf{s}_i), T_s; \mathbf{s}_i, \mathbf{r}) \right]. \tag{28}$$

which generalizes the cases of joint FATT and hypocenter based on AD or DD traveltime data misfit $\mathcal{D}$. Obtaining the gradients of $\mathcal{J}$ with respect to source location requires the determination of $\nabla t(\mathbf{s}_i)$. Because the traveltime field at the source location is a singularity, a direct computation of ∇t at $\mathbf{s}_i$ is not mathematically meaningful. Therefore in LATTE, we exchange the location of source and receivers $(\mathbf{s}, \mathbf{r})$ to $(\hat{\mathbf{r}}, \hat{\mathbf{s}})$ during inversion and invert for the location of the virtual receiver $\hat{\mathbf{r}}$ instead:

$$\mathcal{J}(v_p, v_s, \hat{\mathbf{r}}, \zeta_0) = \frac{1}{2} \sum_{i=1}^{N_{\hat{s}}} \left[\mathcal{D}(t_p + \zeta_0(\hat{\mathbf{r}}), T_p; \hat{\mathbf{s}}_i, \hat{\mathbf{r}}) + \mathcal{D}(t_s + \zeta_0(\hat{\mathbf{r}}), T_s; \hat{\mathbf{s}}_i, \hat{\mathbf{r}}) \right], \tag{29}$$

where $\zeta_0(\hat{\mathbf{r}})$ is the virtual receiver's base time, which varies from virtual receiver to virtual receiver, but each virtual receiver's ζ_0 is consistent over different virtual sources. Exchanging sources and receivers requires an additional step prior to tomography; especially, one has to find all the unique virtual sources and virtual receivers and assign correspondingly the original traveltime to these sources and receivers. In LATTE, we implement this step by leveraging message passing interface (MPI) based distributed-memory parallelism to reduce computational time.

The AD misfit function applies to joint velocity tomography and source location in equation (28) and equation (29). However, we remark that in this case, because the source and receivers are exchanged, for a common-virtual-source gather, the virtual receiver base time $\zeta_0(\hat{\mathbf{r}})$ (or real origin time $\eta_0(\mathbf{s}_i)$) differ from trace to trace. Therefore, in this case, $\zeta_0(\hat{\mathbf{r}})$ must be inverted, and the DD misfit function can no longer eliminates the common origin time for common-virtual-receiver gather as for common-real-source gather. The observation means that for joint tomography and source location, if one uses AD misfit function and if in practice the actual $\eta_0(\mathbf{s})$ are unknown, one must estimate η_0 along with estimating source location.

To apply DD to source location meanwhile avoiding inverting for the unknown η_0, we define a similar but different misfit function. Taking the acoustic case as an example, the DD misfit function for joint tomography and location should read

$$\mathcal{J}_{\mathrm{DD}}(v_p, \hat{\mathbf{r}}) = \frac{1}{2} \sum_{i=1}^{N_{\hat{s}}} \sum_{j=1}^{N_{\hat{r}}} \sum_{k=1}^{N_{\hat{s}}} \left[(t_p(v_p, \hat{\mathbf{s}}_i, \hat{\mathbf{r}}_j) - t_p(v_p, \hat{\mathbf{s}}_k, \hat{\mathbf{r}}_j)) - (T_p(\hat{\mathbf{s}}_i, \hat{\mathbf{r}}_j) - T_p(\hat{\mathbf{s}}_k, \hat{\mathbf{r}}_j)) \right]^2. \quad (30)$$

Note that the innermost summation for each virtual receiver is defined to integrate all the virtual sources. This contrasts with DD-FATT where the summation for each virtual receiver is defined to integrate all the virtual receivers. In fact, it is no longer possible to invert for η_0 with source-receiver-exchanged DD-TLOC because η_0 is not a part of the misfit function.

In this case, the residual for a virtual receiver $\mathbf{r}_j$ is

$$\Gamma(t, T, \hat{\mathbf{s}}_i, \hat{\mathbf{r}}_j) = \sum_{k=1}^{N_{\hat{s}}} \left[(t_p(v_p, \hat{\mathbf{s}}_i, \hat{\mathbf{r}}_j) - t_p(v_p, \hat{\mathbf{s}}_k, \hat{\mathbf{r}}_j)) - (T_p(\hat{\mathbf{s}}_i, \hat{\mathbf{r}}_j) - T_p(\hat{\mathbf{s}}_k, \hat{\mathbf{r}}_j)) \right]. \quad (31)$$

In the following, we distinguish the two cases with $\mathcal{J}_{\mathrm{AD}}$ and $\mathcal{J}_{\mathrm{DD}}$, respectively.

Leveraging the derivations in Tong (2021a) developed for acoustic media, we derive the gradients of $\mathcal{J}_{\mathrm{AD}}$ with respect to the source parameters for elastic media as

$$\frac{\partial \mathcal{J}_{\mathrm{AD}}}{\partial s_x}(\mathbf{s}_j) = \frac{\partial \mathcal{J}}{\partial \hat{r}_x}(\hat{\mathbf{r}}_j) = \sum_{i=1}^{N_{\hat{s}}} \left[\frac{\partial t_p}{\partial x} \Delta(t_p + \zeta_{0,j}, T_p; \hat{\mathbf{s}}_i, \hat{\mathbf{r}}_j) + \frac{\partial t_s}{\partial x} \Delta(t_s + \zeta_{0,j}, T_s; \hat{\mathbf{s}}_i, \hat{\mathbf{r}}_j) \right] \delta(\mathbf{x} - \hat{\mathbf{r}}_j), \quad (32)$$

$$\frac{\partial \mathcal{J}_{\rm AD}}{\partial s_y}(\mathbf{s}_j) = \frac{\partial \mathcal{J}}{\partial \hat{r}_y}(\hat{\mathbf{r}}_j) = \sum_{i=1}^{N_{\hat{s}}} \left[\frac{\partial t_p}{\partial y} \Delta(t_p + \zeta_{0,j}, T_p; \hat{\mathbf{s}}_i, \hat{\mathbf{r}}_j) + \frac{\partial t_s}{\partial y} \Delta(t_s + \zeta_{0,j}, T_s; \hat{\mathbf{s}}_i, \hat{\mathbf{r}}_j) \right] \delta(\mathbf{x} - \hat{\mathbf{r}}_j), \tag{33}$$

$$\frac{\partial \mathcal{J}_{\rm AD}}{\partial s_z}(\mathbf{s}_j) = \frac{\partial \mathcal{J}}{\partial \hat{r}_z}(\hat{\mathbf{r}}_j) = \sum_{i=1}^{N_{\hat{s}}} \left[\frac{\partial t_p}{\partial z} \Delta(t_p + \zeta_{0,j}, T_p; \hat{\mathbf{s}}_i, \hat{\mathbf{r}}_j) + \frac{\partial t_s}{\partial z} \Delta(t_s + \zeta_{0,j}, T_s; \hat{\mathbf{s}}_i, \hat{\mathbf{r}}_j) \right] \delta(\mathbf{x} - \hat{\mathbf{r}}_j), \tag{34}$$

$$\frac{\partial \mathcal{J}_{\rm AD}}{\partial \eta_0}(\mathbf{s}_j) = \frac{\partial \mathcal{J}}{\partial \zeta_0}(\hat{\mathbf{r}}_j) = \sum_{i=1}^{N_{\hat{s}}} \left[\Delta(t_p + \zeta_{0,j}, T_p; \hat{\mathbf{s}}_i, \hat{\mathbf{r}}_j) + \Delta(t_s + \zeta_{0,j}, T_s; \hat{\mathbf{s}}_i, \hat{\mathbf{r}}_j) \right] \delta(\mathbf{x} - \hat{\mathbf{r}}_j), \tag{35}$$

The above equations indicate that in either acoustic or elastic media, the gradients of $\mathcal{J}_{\rm AD}$ with respect to each of the source parameters (s_x, s_y, s_z, η_0) for each virtual receiver (or true source) is a scalar value summing from the contributions of all virtual sources (or true receivers).

In the case of DD-TLOC, the gradients of misfit function with respect to source location based on both P- and S-arrival traveltime are given by

$$\frac{\partial \mathcal{J}_{\rm DD}}{\partial s_x}(\mathbf{s}_j) = \frac{\partial \mathcal{J}_{\rm DD}}{\partial \hat{r}_x}(\hat{\mathbf{r}}_j) = \sum_{i=1}^{N_{\hat{s}}} \left[\frac{\partial t_p}{\partial x} \Gamma(t_p, T_p; \hat{\mathbf{s}}_i, \hat{\mathbf{r}}_j) + \frac{\partial t_s}{\partial x} \Gamma(t_s, T_s; \hat{\mathbf{s}}_i, \hat{\mathbf{r}}_j) \right] \delta(\mathbf{x} - \hat{\mathbf{r}}_j), \tag{36}$$

$$\frac{\partial \mathcal{J}_{\rm DD}}{\partial s_y}(\mathbf{s}_j) = \frac{\partial \mathcal{J}_{\rm DD}}{\partial \hat{r}_y}(\hat{\mathbf{r}}_j) = \sum_{i=1}^{N_{\hat{s}}} \left[\frac{\partial t_p}{\partial y} \Gamma(t_p, T_p; \hat{\mathbf{s}}_i, \hat{\mathbf{r}}_j) + \frac{\partial t_s}{\partial y} \Gamma(t_s, T_s; \hat{\mathbf{s}}_i, \hat{\mathbf{r}}_j) \right] \delta(\mathbf{x} - \hat{\mathbf{r}}_j), \tag{37}$$

$$\frac{\partial \mathcal{J}_{\rm DD}}{\partial s_z}(\mathbf{s}_j) = \frac{\partial \mathcal{J}_{\rm DD}}{\partial \hat{r}_z}(\hat{\mathbf{r}}_j) = \sum_{i=1}^{N_{\hat{s}}} \left[\frac{\partial t_p}{\partial z} \Gamma(t_p, T_p; \hat{\mathbf{s}}_i, \hat{\mathbf{r}}_j) + \frac{\partial t_s}{\partial z} \Gamma(t_s, T_s; \hat{\mathbf{s}}_i, \hat{\mathbf{r}}_j) \right] \delta(\mathbf{x} - \hat{\mathbf{r}}_j), \tag{38}$$

with the DD misfit function Δ defined in equation (30). Again, the gradients of $\mathcal{J}_{\rm DD}$ with respect to each of the source location (s_x, s_y, s_z) for each virtual receiver (or true source) is a scalar value summing from the contributions of all virtual sources (or true receivers).

In LATTE, we invert for source parameters (including spatial location, and source origin time, if necessary) in the same manner as for model parameters. Therefore, the inversion scheme developed for model parameters seamlessly apply to source parameters inversion as well, resulting in a more consistent inversion scheme. This is contrast to the hybrid local-global inversion scheme by Tong (2021a). More importantly, such a consistent inversion scheme enables a more flexible way to regularize an inversion using the model and source regularization schemes that will be detailed in the next section.

It should be noted that in the joint tomography-location, we again compute the optimal step size using the small-perturbation strategy. However, in this case, we misfit vectors are

$$\beta_{i,j}(m,\mathbf{s}) = \Delta\left(t(m^{(l-1)}+\epsilon\Delta m^{(l)},\hat{\mathbf{r}}_j^{(l-1)}+\Delta\hat{\mathbf{r}}_j^{(l)}), t(m^{(l-1)},\hat{\mathbf{r}}_j^{(l-1)});\hat{\mathbf{s}}_i\right), \tag{39}$$

$$\gamma_{i,j}(m,\mathbf{s}) = \Delta\left(T, t(m^{(l-1)},\hat{\mathbf{r}}_j^{(l-1)});\hat{\mathbf{s}}_i\right), \tag{40}$$

where $\Delta\hat{\mathbf{r}}_j^{(l)}$ represents the search direction of the virtual receiver (or real source) locations of the l-th iteration. Correspondingly, the update of the model and source parameters are

$$v_p^{(l)} = v_p^{(l-1)} + \alpha^{(l)}\Delta v_p^{(l)}, \tag{41}$$

$$v_s^{(l)} = v_s^{(l-1)} + \alpha^{(l)}\Delta v_s^{(l)}, \tag{42}$$

$$\hat{\mathbf{r}}_j^{(l)} = \hat{\mathbf{r}}_j^{(l-1)} + \alpha^{(l)}\Delta\hat{\mathbf{r}}_j^{(l)}. \tag{43}$$

Similarly, if one needs to solve for the origin time η_0, then β and γ should be computed by properly considering the perturbation of η_0 under search direction $\Delta\eta_0$ like $\hat{\mathbf{r}}_j$: $t(m^{(l-1)}+\epsilon\Delta m^{(l)},\hat{\mathbf{r}}_j^{(l-1)}+\Delta\hat{\mathbf{r}}_j^{(l)},\eta_{0,j}^{(l-1)}+\Delta\eta_{0,j}^{(l)})$.

2.4 Model and source parameter regularization

For both functionalities that involve model parameter update (i.e., FATT and TLOC), we develop a novel model parameter regularization to improve the geological fidelity of the inversion results. The model parameter regularizer consists of a total generalized p-variation regularizer (Gao and Huang, 2019) and a P/S wave velocity structure similarity regularizer. In addition, for TLOC, we introduce a novel source parameter regularizer based on a end-to-end, supervised ML model to improve the geological fidelity of inverted source locations.

Specifically, we define the regularized joint tomography-location as a hybrid optimization problem:

$$\begin{aligned}\mathcal{J}(v_p,v_s,\mathbf{s},\eta_0) = {} & \sum_{i=1}^{N_s}\mathcal{D}(t_p,T_p;\mathbf{s},\eta_0) + \sum_{i=1}^{N_s}\mathcal{D}(t_s,T_s;\mathbf{s},\eta_0) \\ & + \omega_{v_p}\mathcal{T}(v_p) + \omega_{v_s}\mathcal{T}(v_s) + \omega_{v_p/v_s}\|1-\mathcal{S}(v_p,v_s)\|^2 \\ & + \omega_s\|\mathcal{F}(\mathbf{s})\|^2,\end{aligned} \tag{44}$$

where for convenience, we drop the coefficient $\frac{1}{2}$ associated with every misfit term.

The operator $\mathcal{T}$ is an ℓ_p-norm minimization problem defined as (Knoll et al., 2011; Gao and Huang, 2019):

$$\mathcal{T}(v_p) = \min_m\left\{\alpha_1\|\nabla v_p - m\|_p^p + \alpha_2\|\varepsilon(m)\|_p^p\right\} \tag{45}$$

with the norm $0 \leq p \leq 1$, and α_1 and α_2 are weighting factors for the first- and second-order total variations, respectively. In 3D, the gradient matrix $\varepsilon(m)$ for a vector field $m = (m_x, m_y, m_z)$ reads

$$\varepsilon(m) = \begin{bmatrix} \nabla_x m_x & \frac{1}{2}(\nabla_x m_y + \nabla_y m_x) & \frac{1}{2}(\nabla_x m_z + \nabla_z m_x) \\ \frac{1}{2}(\nabla_x m_y + \nabla_y m_x) & \nabla_y m_y & \frac{1}{2}(\nabla_y m_z + \nabla_z m_y) \\ \frac{1}{2}(\nabla_x m_z + \nabla_z m_x) & \frac{1}{2}(\nabla_y m_z + \nabla_z m_y) & \nabla_z m_z \end{bmatrix}. \tag{46}$$

The operator $\mathcal{S}$ measures the similarity between v_p and v_s, by which we intend to improve the structural similarity between updated v_p and v_s. Although there are sophisticated structure similarity operators, in LATTE, we impose the similarity simply through constraining and smoothing the ratio between v_p and v_s, i.e., v_p/v_s.

We also impose a source regularization term through $\mathcal{F}$, which is a misfit function that minimizes the spatial spreading of source locations. In other words, we want the inverted seismicity locations to be "focused" as much as possible. However, we do not want all the inverted seismicity converges to a single spatial location by the regularizer $\mathcal{F}$; otherwise, the solution will be of low seismological fidelity. In LATTE, we focus on fault/fracture-related seismicity, and therefore intend to develop a regularizer that improve the consistency between the inverted source locations with one or multiple fault/fracture surfaces.

It is essentially difficult to compute the gradient $\partial\mathcal{T}/\partial v_p$ or $\partial\mathcal{T}/\partial v_s$ as $\mathcal{T}$ itself is defined through an optimization problem rather than an analytical equation. The same challenge occurs to computing $\partial\mathcal{F}/\partial\mathbf{s}$, because $\mathcal{F}$ does not have an analytical expression. To solve the regularized inversion problem, we convert regularized optimization in equation (44) to an alternating-direction optimization:

$$\begin{aligned} v_p^{(l+1)}, v_s^{(l+1)}, \mathbf{s}^{(l+1)} &= \underset{v_p, v_s, \mathbf{s}}{\arg\min} \sum_{i=1}^{N_s} \mathcal{D}(t_p + \eta_0, T_p) + \sum_{i=1}^{N_s} \mathcal{D}(t_s + \eta_0, T_s) \\ &\quad + \omega_{v_p} \| v_p - m_p^{(l)} \|^2 + \omega_{v_s} \| v_s - m_s^{(l)} \|^2 + \omega_{v_p/v_s} \left\| \frac{v_p}{v_s} - r^{(l)} \right\|^2 \\ &\quad + \omega_s \| \mathbf{s} - \sigma^{(l)} \|^2, \end{aligned} \tag{47}$$

$$m_p^{(l+1)} = \underset{m_p}{\arg\min}\, \gamma_{v_p} \mathcal{T}(m_p) + \omega_{v_p} \| v_p^{(l+1)} - m_p \|_2^2, \tag{48}$$

$$m_s^{(l+1)} = \underset{m_s}{\arg\min}\, \gamma_{v_s} \mathcal{T}(m_s) + \omega_{v_s} \| v_s^{(l+1)} - m_s \|_2^2, \tag{49}$$

$$r^{(l+1)} = \underset{r}{\arg\min}\, \omega_{v_p/v_s} \left\| \mathcal{S}\left(\frac{v_p^{(l+1)}}{v_s^{(l+1)}} \right) - r \right\|_2^2, \tag{50}$$

$$\sigma^{(l+1)} = \underset{\sigma}{\arg\min}\, \omega_s \| \mathcal{F}(\mathbf{s}^{(l+1)}) - \sigma \|^2. \tag{51}$$

The first optimization problem is simply first-arrival traveltime tomography (or joint tomography-location) by adding $v_p - m_p^{(l)}$, $v_s - m_s^{(l)}$, or $\mathbf{s} - \sigma^{(l)}$ to the gradients of model parameters or source parameters in each iteration, respectively. This will gradually guide the model and source parameters converge to $m_p^{(l)}$, $m_s^{(l)}$, and $\sigma^{(l)}$, respectively, which are solved via the following optimization problems.

The second and third optimization problems are TGpV image denoising problems. We solve $\mathcal{T}$ optimization (TGpV 2D and 3D image denoising) using the algorithm in Gao and Huang (2019), with an open-source implementation we developed in Gao and Chen (2024). The input to the optimization is the updated v_p or v_s model, while the output is "denoised" or "regularized" v_p or v_s model.

The fourth optimization is not a strict minimization problem, but to impose a constraint $\mathcal{S}$ on v_p and v_s so that they are structurally similar. There are many choices for this constraint. In LATTE, $\mathcal{S}$ composes of three operations: box limiting, median filtering, and Gaussian smoothing. The box limiting $\mathcal{B}_a^b$ constraints the ceiling and floor values for the ratio v_p/v_s, which mimics the fact that in practice this value is generally not arbitrary but lies within a range $[a, b]$. While for different geologies or materials this range can be different, in practice the approximate values of a and b are not completely unknown. The other operations, including a median filtering $\mathcal{M}$ and a Gaussian smoothing $\mathcal{G}_\sigma$, reduce abrupt spatial variations of v_p/v_s, making v_p and v_s closer in structures. The standard deviation σ is a hyper-parameter that can be chosen differently for different models depending on a user's preference. Alternatively, one can also use more sophisticated smoothing, such as structure-oriented nonlinear anisotropic diffusion (Wu and Guo, 2018), to smooth the ratio. In our code, we find the composite operation $\mathcal{S} = \mathcal{G}_\sigma \circ \mathcal{M} \circ \mathcal{B}_a^b$ suffices the purpose of similarizing v_p and v_s.

Similarly, the fifth optimization, i.e., the source parameter regularization problem $\mathcal{F}$, is not a strict optimization problem. The purpose of this optimization is to improve the spatial correlation among the inverted seismicity locations. For geophysical applications, seismicity does not occur randomly, and in general the locations of seismicity are strongly correlated with faults or fractures. Therefore, we want the inverted source locations fall on one or multiple faults/fracture surfaces as much as possible, effectively making $\mathcal{F}$ a fault geometry constraint for seismicity. For other types of applications where sources do not essentially correlate with faults/fractures, and we can conveniently ignore this fault geometry constraint by setting $\omega_s = 0$.

The fault constraint is not trivial to solve. For instance, one can use automatically clustering algorithms to cluster inverted seismicity locations, and then use some surface fitting algorithm to move the clustered events to a plane or surface. However, it is very challenging to develop an adaptive clustering algorithm that works generally well for different scenarios, especially when the locations distribute irregularly with drastically different densities in space. Instead, we solve this fault constraint problem using a supervised machine learning model. At each iteration, we convert the source locations $\mathbf{s}^{(l+1)}$ to a 2D or 3D grid-based image using a maximum-limiting summation of Gaussian functions:

$$I(\mathbf{x}) = \max_{i=1,N_{\hat{r}}} \exp\left(-\frac{\|\mathbf{x}-\mathbf{s}_i\|^2}{2\sigma^2}\right), \tag{52}$$

where we omit the superscript $(l+1)$ for simplicity, $\|\cdot\|$ represents L_2 norm, and σ represents the standard deviation of the Gaussian function. In our code, we set $1/2\sigma^2 = 0.3$, resulting in an annihilating amplitude approximately eight or nine grid points away from the source location.

We develop an iterative, multitask ML model shown in Figure 32 of Appendix C to infer and refine faults and fault attributes (including probability, dip, strike) from a source image. Specifically, this ML models contains two neural networks (NN): a multitask inference NN and a multitask refinement NN. The multitask inference ML model is an end-to-end model where the output has the same dimensions as the input source image. The multitask refinement ML model is also an end-to-end model, but the input to this refinement NN contains the source image and the inferred fault attributes, which might be "noisy" or "broken" due to imbalanced source locations. By applying the refinement NN several times based on the results obtained from a previous iteration, we obtain cleaner, continuous, and thus more interpretable faults compared with the ones generated from the multitask inference NN. Upon obtaining the fault attributes, we generate a fault-constrained source image by moving every source $\mathbf{s}_i$ to the nearest fault point in terms of Euclidean distance and use the fault-constrained source locations to guide the iterative source location. Therefore, over iterations, the source locations become more topologically meaningful in terms of correlation with fault/fracture surfaces, resulting in better seismological or geological interpretability. The two objects (source image and fault image) mutually improve each other through the ML model, facilitating the update of source locations for TLOC.

In a qualitative manner, our ML-based source parameter regularization for the l-th iteration could be represented as

$$\begin{aligned} &\text{updated source location}\,\mathbf{s}^{(l)} \rightarrow \text{multitask inference} \\ &\qquad \rightarrow \underbrace{\text{multitask refinement}}_{\text{repeat } N \text{ times}} \rightarrow \text{regularized location}\,\sigma^{(l)}. \end{aligned} \tag{53}$$

The regularization procedure will generate $\sigma^{(l)}$ that essentially falls on a fault/fracture surface, and act as a guidance for updating $\mathbf{s}^{(l+1)}$ in the next iteration. Eventually, $\mathbf{s}^{(N)} \approx \sigma^{(N)}$ at the end of a TLOC inversion.

3 Numerical results

3.1 Traveltime computation

We first use a synthetic velocity model to validate the traveltime computation functionalities of LATTE.

LATTE enables both first-arrival traveltime computation and reflection traveltime computation. Figures 1a and b display the v_p and v_s models with low and high velocity anomalies, respectively. Figure 1c displays two reflectors (represented by values 1 and 2, respectively).

Figures 2 displays the first P-arrival traveltime field for a source placed at the horizontal position of 0.3 km. The gradient in the velocity model causes notable diving wave features in the traveltime field. Figures 2b and c display the PP-arrival traveltime fields associated with the first and second reflectors, respectively. Note that below each reflector, the computed traveltime field does not represent reflection but transmission traveltime. Therefore, the traveltime field below each reflector is the same with the first-arrival traveltime in Figure 2a. Figures 2d and e display the PS-arrival traveltime fields associated with the first and second reflectors, respectively. In this case, the traveltime field below each reflector represents PS transmission arrival traveltime, and they are not the same with the PP transmission arrival traveltime displayed in Figure 2a.

Figure 3a displays the first-arrival traveltime field. Figures 3b and c display the SP reflection traveltime fields, where the traveltime field below each reflector represents SP transmission arrival traveltime field. Similarly, Figures 3d and e display the SS reflection traveltime fields, where the traveltime field below each reflector represents SS transmission arrival traveltime, and is consistent with the values displayed in Figure 3a.

Figures 4a and b display the traveltime recorded at the surface of the validation model. We observe that in this case because $v_p/v_s > 1$ in the entire model, PP1 and PP2 (representing the PP reflection traveltime from reflectors 1 and 2, respectively) arrivals are always earlier than PS reflection traveltime (PS1 and PS2); at large offsets, the PP reflections may arrive earlier then the first-arrival traveltime, which is essentially a mixture of direct wave at near offsets and diving wave arrivals at large offsets.. By contrast, for SS source, the SP reflections arrive notably earlier than both the “first-arrival” traveltime and the SS reflection traveltime field. The results indicate that for elastic media characterization, picking first-arrival S traveltime can be very challenging depending on the geometry. At large offsets, SP component may arrive much earlier than other components, and the true “first-arrival” S-wave may be obscured in noisy waveforms.

3.2 First-arrival traveltime tomography

We use a near-surface faulted model to demonstrate the efficacy of AD-FATT and DD-FATT implementation in our LATTE.

Figure 5a displays a faulted velocity model with a horizontal span of 4 km and a maximum depth of 500 m. We set a number of structural complexities of the layers including anticlines, inclines, and faults. We also set a low velocity value (600 m/s) for the three faults. The model consists of 51 grid points in the depth direction, with a grid spacing of 10 m, and with 401 grid points in the horizontal direction, with a grid spacing of 10 m. Figure 5b displays a smooth velocity model (1D linear gradient) model as the initial model for both AD-FATT and DD-FATT. All the important features of the ground-truth velocity model are invisible on this initial velocity model. We place a total of 40 sources on the top surface of the model, starting from 50 m and with a uniform horizontal spacing of 100 m. We place a total of 401 receivers on the top surface, with a uniform horizontal spacing of 10 m. For both inversions, we apply energy preconditioning to the gradient and adopt the NCG inversion scheme to obtain the search direction.

Figures 6a and b display the inverted v_p models by AD-FATT and DD-FATT, respectively, both after 100 iterations. Meanwhile, Figure 7 displays the normalized data misfit convergence curves of AD-FATT and DD-FATT using blue and red curves, respectively. Both inversions correctly recover the low-wavenumber features of the ground-truth model. However, both inversion results indicate that it could be very challenging to accurately delineate high-resolution features based solely on first-arrival traveltime, even though both AD-FATT and DD-FATT converge to a low data misfit. For instance, both inversions miss the deep part of two low-velocity faults between 2 km to 3.5 km at the horizontal position, although both correctly recover the shallow part of the faults.

Figure 8a displays a comparison between the ground-truth and synthetic traveltime in the initial 1D velocity model for the second source at 20 m. Figures 8b and c show the ground-truth and synthetic traveltime for the same source in the inverted velocity models obtained using AD-FATT and DD-FATT, respectively. We observe that both inversions generate an accurate first-arrival traveltime match after 100 iterations. We also display the distribution of traveltime misfit in the inverted model for AD-FATT and DD-FATT in Figures 8d and e, respectively. Through the statistics, we find that DD-FATT results in slightly more consistent traveltime for a total of 16,040 traveltime measurement, even though it uses differential traveltime rather than absolute traveltime for residual and misfit computation.

The results demonstrate the efficacy of AD-FATT and DD-FATT functionalities implemented in LATTE.

3.3 Source location and joint tomography-location

Next, we validate our method and implementation of traveltime-based source location, as well as joint tomography-location, in LATTE. Same as in the last example, we validate both AD and DD misfit functions, and we use AD-TLOC and DD-TLOC to denote these two cases. As we described in the methodology, we exchange sources and receivers for source location, indicating that the receivers ar not placed on the surface of the model. The tomography results displayed below will therefore demonstrate the validity of our arguments on placing receivers at arbitrary positions of a model as detailed in Appendix B.

We use an elastic checkerboard model and both P- and S-arrival traveltime in this test. Figure 9a displays the ground-truth v_p model, and the S-wave velocity model is set to $v_s = v_p/\sqrt{3}$ for simplicity. The dimension of the model is 3 km in the depth direction and 4 km in the horizontal direction. The grid spacing is 10 m in both directions. We set a total of 300 randomly distributed sources within the model, and a total of 50 receivers on the top surface, starting from 50 m and with a uniform horizontal spacing of 100 m. In addition, we set random origin time η_0 ranging from 0 to 100 s for the 300 sources. We generate traveltime using the parallel fast-sweeping elastic eikonal solver implemented in LATTE.

In the first test for this checkerboard model, we use AD-TLOC to simultaneously invert for the source location and origin time by assuming known velocity models. Figure 10a displays the ground-truth location of the 300 sources in space. For validating AD-TLOC, we set the initial guess of location of all sources at the center of the model as denoted by the red dot. We also set the initial guess of origin time η_0 to be the mean of all ground-truth η_0 which is approximately 50 s.

Figures 10b-c display the inverted source locations at the 5th, 10th, and 100th iterations, respectively, where we use gray lines to connect the ground-truth and inverted source locations. We observe that the inverted source locations gradually converge to their ground-truth positions. Sources in the deep and boundary regions of the model appear to have slightly larger errors because of the insufficient traveltime field coverage and stacking in these regions.

Figure 11a displays the comparison among the ground-truth origin time, the initial guess, and the inverted origin time of the 300 sources. The inversion result indicates that AD-TLOC correctly estimates the origin time given a trivial initial guess (a same value for all sources). Figure 11b displays the comparison among the ground-truth T_p subtracting the ground-truth origin time (i.e., $T_p - \eta_0$, blue curve), the synthetic t_p in the initial smooth velocity model (i.e., $t_p^{(l=0)}$, green curve), and the synthetic t_p in the inverted velocity in the inverted model ((i.e., $t_p^{(l=100)}$ red curve), all corresponding to the second virtual source. Similarly, Figure 11c displays the comparison for S-arrival traveltime, where we observe a similar level of accuracy. Common-virtual-source gathers at other locations show similar level of error with the ones displayed in Figures 11b and c. The consistency between the traveltime computed in the inverted model and the ground-truth traveltime validates the efficacy and accuracy of AD-TLOC in LATTE.

In the second test for this checkerboard model, we perform DD-TLOC by again assuming know velocity models. We set a trivial initial guess for the location of all sources – the center of the model. In the test, we only invert for the source locations. As we described in the text, using DD-only misfit functions, we cannot invert for the origin time as η_0 is eliminated by the DD misfit function for each real-source gather (or virtual-receiver gather).

Figure 12a displays the ground-truth and initial guess of the source locations, while Figures 12b-d show the inverted source locations in the 5th, 10th, and 100th iterations, respectively. Comparing with the AD-TLOC inversion results shown in Figures 10b-d, we find that by eliminating the common origin time, DD-TLOC results in an more accurate estimation of source location for almost all the sources. There are several sources in the deep part of the model that are not well located, but these sources are also furthest away from the receivers. The differential traveltime misfits associated with these sources are also the smallest, resulting a suboptimal update of these deep sources.

Figure 13a displays the comparison among the ground-truth $t_p - \eta_0$, $t_p^{(l=0)}$, and $t_p^{(l=100)}$. Even though we use DD misfit function rather than AD misfit function, we observe a good consistency between the observed and the synthetic traveltime. In fact, the traveltime misfits associated this common-virtual-source gather is better than that in the AD-TLOC displayed in Figure 11b. The consistency of S-arrival traveltime displayed in Figure 13b is at a similar level with the P-arrival traveltime, and again is higher than that generated by AD-TLOC displayed in Figure 11c. The results validate the efficacy and accuracy of DD-TLOC in LATTE, and demonstrate the advantage of DD-TLOC over AD-TLOC in leveraging differential time to improve source location accuracy.

In the third test for this checkerboard model, we perform simultaneous velocity tomography and source location using DD-TLOC. We assume homogeneous initial velocity models $v_p^{(l=0)} = 2000$ m/s and $v_s^{(l=0)} = 2000/\sqrt{3}$ m/s, and set the initial guess of source location to be $(x_0, z_0) = (\mu(s_x), 2980)$ m where we use $\mu(s_x)$ to denote the average value of the horizontal positions of all sources. Because seismic velocity and source location are strongly coupled in in terms of traveltime, and in this test we only have surface receivers, we anticipate a poorer source location result compared with those of the first two tests.

Figures 14a and b display the inverted v_p and v_s models by DD-TLOC, respectively. Compared with the ground-truth model in Figure 9, we find that the central part of the model is relatively better recovered than the regions in the deep and boundary regions. This is probably because the background model is a homogeneous model for both v_p and v_s, therefore there is not diving wave/traveltime field to leverage for updating the deep region.

Figure 15a compares the ground-truth and the initial source locations, while Figures 15b-c compared the ground-truth and inverted source locations in the 5th, 10th, and 100th iterations, respectively. Comparing the inverted source locations with that in Figure 10d where the velocity model is known, we observe that inaccurate velocity models introduce a notable challenge to source location. In this case, the sources in the deep and boundary regions show notably higher level of error than those in the known-velocity case. The inaccuracy is consistent with the low accuracy of inverted velocity models displayed in Figure 15.

Figure 16 compares the ground-truth traveltimes $t_p - \eta_0$ and $t_s - \eta_0$ with synthetic traveltimes associated with the second virtual source. We observe visually higher standard deviations for both P- and S-arrival traveltimes compared with those in the first two tests.

The above results indicate the limitation of DD-TLOC for joint tomography-location in an elastic model with poor initial guesses of velocity models and source locations. Comparing the results with those in the location-only tests, we find that velocity uncertainty can deteriorate the accuracy of source location. Because velocity and source location are strongly coupled, the influence is essentially mutual and cannot be straightforwardly decoupled.

In the last part of the Methodology section, we introduced model parameter regularization consisting of TGpV and $v_p - v_s$ similarity regularizers to FATT and TLOC. For this model, because the source locations are purely random, the ML-based source parameter regularization does not apply – there is no fault that the sources can align to. In the fourth test, therefore, we validate the efficacy of the model parameter regularization by setting $\omega_s = 0$.

Figure 17 display the inverted v_p and v_s models in the 100th iterations using the regularized DD-TLOC joint tomography-location functionality. Compared with those without model parameter regularization displayed in Figure 14, we find that model parameter regularization notably reduces random-noise-like artifacts in the inversion results. The pattern of checkerboard in this case becomes clearer, more closely resembling the ground-truth model in Figure 9. Similar with the case without model parameter regularization, the most well-recovered region is the central part of the model, with less accurate recovery of velocity perturbation in the deep and boundary regions. We must remind that the inaccuracy is not intrinsic to FATT or TLOC in LATTE. Any tomography methods may encounter similar issue as the inaccuracy is essentially determined by the poor illumination of these regions with a surface-only receiver distribution.

Figure 18 display the initial and inverted source locations using regularized DD-TLOC. Although in this case the sources in the deep and boundary regions still cannot be well located, visually the errors are smaller compared with those in Figure 15. Because we do not regularize source parameters in this test, the improvement of location accuracy is essentially introduced by the better-resolved velocity models.

Lastly, the traveltime comparison in Figure 19 further demonstrates the improvement in traveltime consistency introduced by regularized DD-TLOC functionality compared with plain DD-TLOC.

3.4 Fault-constrained source location

In the fourth example, we demonstrate the efficacy of fault-constrained source location functionality in LATTE.

Figure 20a displays a 2D v_p model of 3 km in the depth direction and 5 km in the horizontal direction. The model consists of a smoothly varying upper part and faulted structures in the lower part. Figure 20b displays a Gaussian-smoothed velocity model for locating the sources.

We set a total of 50 receivers on the surface, starting from 50 m and with a uniform interval of 100 m, and also set 30 receivers at the horizontal position of 2 km, starting from 100 m in depth, and with a uniform interval of 60 m. The vertically distributed receivers mimic the scenario of receivers placed in a well. We set a total of 1,200 sources along the faults in the lower half, mimicking the scenario of fracturing-induced seismicity. Same with the previous tests, we assume a trivial initial source location in the center of the lower half model at $(x_0, z_0) = (2500, 2500)$ m.

To improve reality, we assign random values ranging from 0 to 10 s as the origin time for these 1,200 sources and use DD-TLOC to invert for the source locations. In this test, we do not update the velocity. However, we add smoothed random noise to the computed traveltime in the ground-truth model to mimic imperfect traveltime picking in practice, as displayed in Figure 21. The maximum value of the added noise in all common-source gathers is 20 ms. Translating to spatial distance under this velocity model, the noise generates up to approximately 50-m random errors in space for each source.

As we point out in the Methodology, one may want to avoid an "early kick-in" when the source locations are still far away from the truth locations. In practice, one may need to use experience to decide when to regularize source parameters. We start to regularize source location update using the ML-based regularizer starting from the 16th iteration. Figures 22a and b display the initial source location and the updated source locations in the 5th iteration. Figures 22c and d display the inverted source locations by plain DD-TLOC and fault-constrained DD-TLOC, respectively. It is visually evident that, without fault constraint for source location, the noise in the data can affect the accuracy of location, even though both inversions can converge in terms of data misfit. In the deep and boundary regions, located sources can smear into each other, making it difficult to correlate the located sources with individual faults. By contrast, the fault-constrained DD-TLOC results in a more interpretable source location result, where the located sources are mostly aligned with faults and close to their ground-truth locations. In fact, in the fault-constrained location result, we only observe few notable mislocated sources in the lower right corner, and two in the lower left corner. Given better illumination of these regions, it is likely these errors can be further reduced.

Figures 23a and b display the source image and ML-inferred fault dip image in the 5th iteration. At early iterations, the sources are not yet well located, and therefore the inferred faults do not resemble the ground-truth faults denoted by the red points. By contrast, Figures 22c and d display the source image and corresponding ML-inferred fault dip image at the 50th iteration. We observed a good consistency between the source image and the ground-truth source locations, as well as a good consistency between the inferred faults and ground-truth source locations. The results demonstrate that our ML-based source parameter regularization can gradually guide or constrain updated source locations towards faults inferred from the source locations themselves, eventually leading to higher fidelity and interpretability of located source locations.

3.5 Regularized joint tomography and source location

In the final example, we demonstrate the efficacy and accuracy of DD-TLOC joint tomography-location with both model and source parameter regularization for a 3D elastic model.

Figure 24a displays a 3D v_p model. The background variation of this model is a smooth model displayed in Figure 24b with several intersecting faults. The range of background velocity is [1000, 3000] m/s. We add a 3D checkerboard velocity perturbation with a range of $[-300, 300]$ m/s to the background velocity model and obtain the velocity model in Figure 24a. The model is 1 km in depth, 2 km along the Y direction, and 3 km along the X direction. The v_s model follows the same background spatial variation pattern, yet with a different value range from [500, 2000] m/s; the checkerboard perturbation added to the background v_s model has a range of $[-300, 300]/\sqrt{3}$ m/s. Therefore, the resulting v_p and v_s velocity models have nonuniform ratios in space. The background velocity models also serve as the initial velocity model in the following tests.

We display four faults in the upper right corner of Figure 24a. We set a total of 1,200 sources randomly distributed on the faults. We set a total of $R_x \times R_y = 15 \times 10$ receivers on the surface of the model. For this DD-TLOC test, we exchange the sources and receivers for simultaneous velocity update and source location inversion, therefore there are effectively 150 common-virtual-source gathers after reciprocity traveltime data rearrangement.

Similar with the previous example, to mimic practical noise caused by inaccurate phase picking, we add smoothed random noise to the traveltime data simulated in the ground-truth models as displayed in Figure 25. The difference is that for this test, we set a higher maximum amplitude for the noise (50 ms), which intuitively may result in higher uncertainties to the inversions.

Figure 26 display the inverted v_p and v_s models without model or source parameter regularization. We observe that the general heterogeneity pattern of the ground-truth velocity models are revealed in both v_p and v_s. However, there are numerous random velocity perturbations in the inverted models. These artifacts are possibly due to the uneven coverage of the sources and receivers, as well as the random noise in data. By contrast, in Figure 27, we display the inverted models and source locations with simultaneous model and source parameter regularization as described in the

Methodology section. The inverted velocity models are notably cleaner than the ones without model parameter regularization, where we observe almost no random artifacts.

We further compare horizontal slices at two depths among the ground-truth and the inverted velocity perturbations without and with model regularization. Figure 28 display the comparison of a horizontal slices at a depth of 100 m. The regularized DD-TLOC generates a horizontal velocity perturbation with notably piecewise smooth velocity variations than those without model regularization. Figure 29 display a similar comparison for the depth of 340 m, which shows similar improvement by our TGpV model regularization.

We display the map view of the ground-truth source locations in Figure 30a and the initial guess for both inversions in Figure 30. We define the horizontal and vertical errors of an inverted source location as

$$E_h = \sqrt{(s_x - s_{x,0})^2 + (s_y - s_{y,0})^2}, \tag{54}$$

$$E_z = |s_z - s_{z,0}|, \tag{55}$$

where (s_x, s_y, s_z) represents the inverted source location and $(s_{x,0}, s_{y,0}, s_{z,0})$ represents the ground-truth location. Figures 30c and d display the horizontal and vertical errors of the inverted source locations without source parameter regularization. The results show that with only surface receivers, the horizontal locations are more accurately estimated than the vertical locations. If well receivers are available, in principle the vertical errors should reduce. Figures 30e and f display the horizontal and vertical errors of the source locations inverted with DD-TLOC with our ML-based source parameter regularization, which show an improved consistency with the faults compared with those without source regularization, especially at the ends and intersection regions of the faults.

In Figures 31a and b, we compared the ground-truth source locations (blue balls) and the inverted source locations (red balls) without and with ML-based source parameter regularization. It is evident the ML-based source parameter regularization result in an improved location accuracy. Meanwhile, Figures 31c and d display the inferred and refined faults generated by our multitask ML model in the 50th iteration based on the inverted source locations. The consistency between the ground-truth source locations and the estimated faults demonstrates the efficacy of our multitask ML model in serving as an adaptive guide for source location.

The results for this example demonstrate the efficacy of our model and source parameter regularization. We remark that the fault-constrained source parameter regularization does not apply to scenarios where the sources do not correlate to faults or fault-like structures. In those scenarios, it may be possible to develop other types of regularization to improve source location. Investigating the feasibility of such regularization schemes is beyond the scope of this paper.

4 Conclusions

We have developed an open-source, systematic, high-performance implementation of traveltime computation, traveltime-based tomography, and traveltime-based source location based on the eikonal equation and adjoint-state tomography theory for 2D/3D acoustic and elastic media. Specially, to improve the fidelity and interpretability of inverted model parameters and source parameters, we have developed a novel model parameter regularization scheme based on total generalized p-variation and P- and S-wave velocity structure similarity, as well as a source parameter regularization scheme based on multitask machine learning models. We have demonstrated the efficacy and accuracy of our methods and implementation using several synthetic data examples. The results indicate that our implementation can serve as an adaptive computational framework for traveltime computation, velocity tomography, and source location in 2D/3D acoustic and elastic media.

Acknowledgments

The work was supported by Los Alamos National Laboratory (LANL) Laboratory Directory Research and Development (LDRD) project 20240322ER. LANL is managed and operated by Triad National Security, LLC for the U.S. Department of Energy (DOE) National Nuclear Security Administration (NNSA) under contract No. 89233218CNA000001. The research used high-performance computing resources provided by LANL's Institutional Computing (IC) program. The document is approved for public release under LA-UR-24-27806.

Data Availability

The codes (`LATTE`) implementing the methods developed in this work, as well as the parameter files and scripts for reproducing the results, are open-source available at `github.com/lanl/latte_traveltime`. Faulted models in the examples are generated using our open-source package `RGM` (Random Geological Model generation package) available at `github.com/lanl/rgm`. Datasets for training the multitask machine learning models are also generated using `RGM`. Figures in this work are generated using our open-source plotting package `pymplot` (open-source available at `github.com/lanl/pymplot`), visualization toolkit (VTK), and matplotlib.

References

Aki, K., and P. G. Richards, 2002, Quantitative Seismology: University Science Books, Sausalito, California.

Anagaw, A., 2011, Full waveform inversion with total variation regularization: Proceedings of the 2011 CSPG CSEG CWLS Joint Annual Convention, 1–4.

Asnaashari, A., R. Brossier, S. Garambois, F. Audebert, P. Thore, and J. Virieux, 2013, Regularized seismic full waveform inversion with prior model information: Geophysics, **78**, no. 2, R25–R36, doi: 10.1190/geo2012-0104.1.

Bretaudeau, F., R. Brossier, J. Virieux, and L. Métivier, 2014, First-arrival delayed tomography using 1st and 2nd order adjoint-state method: SEG Technical Program Expanded Abstracts 2014, 4757–4762, doi: 10.1190/segam2014-0987.1.

Chambers, K., and J.-M. Kendall, 2008, A practical implementation of wave front construction for 3-D isotropic media: Geophysical Journal International, **173**, no. 3, 1030–1038, doi: 10.1111/j.1365-246X.2008.03790.x.

Chen, Y., Y. Chen, S. Fomel, A. Savvaidis, O. M. Saad, and Y. A. S. I. Oboué, 2023, Pyekfmm: A Python package for 3D fast-marching-based travel-time calculation and its applications in seismology: Seismological Research Letters, **94**, no. 4, 2050–2059, doi: 10.1785/0220230042.

Dando, B. D. E., B. P. Goertz-Allmann, D. Kühn, N. Langet, A. M. Dichiarante, and V. Oye, 2021, Relocating microseismicity from downhole monitoring of the Decatur CCS site using a modified double-difference algorithm: Geophysical Journal International, **227**, no. 2, 1094–1122, doi: 10.1093/gji/ggab255.

de Kool, M., N. Rawlinson, and M. Sambridge, 2006, A practical grid-based method for tracking multiple refraction and reflection phases in three-dimensional heterogeneous media: Geophysical Journal International, **167**, no. 1, 253–270, doi: 10.1111/j.1365-246X.2006.03078.x.

Detrixhe, M., F. Gibou, and C. Min, 2013, A parallel fast sweeping method for the eikonal equation: Journal of Computational Physics, **237**, 46–55, doi: 10.1016/j.jcp.2012.11.042.

Esser, E., L. Guasch, F. J. Herrmann, and M. Warner, 2016, Constrained waveform inversion for automatic salt flooding: The Leading Edge, **35**, no. 3, 235–239, doi: 10.1190/tle35030235.1.

Fang, H., R. D. van der Hilst, M. V. de Hoop, K. Kothari, S. Gupta, and I. Dokmanić, 2019, Parsimonious Seismic Tomography with Poisson Voronoi Projections: Methodology and Validation: Seismological Research Letters, **91**, no. 1, 343–355, doi: 10.1785/0220190141.

Fichtner, A., H.-P. Bunge, H. Igel, A. Fichtner, H.-P. Bunge, and H. Igel, 2006, The adjoint method in seismology: I. Theory: Physics of the Earth and Planetary Interiors, **157**, no. 1, 86 – 104, doi: 10.1016/j.pepi.2006.03.016.

Fomel, S., S. Luo, and H. Zhao, 2009, Fast sweeping method for the factored eikonal equation: Journal of Computational Physics, **228**, no. 17, 6440–6455, doi: 10.1016/j.jcp.2009.05.029.

Gao, K., 2024, Iterative multitask learning and inference from seismic images: Geophysical Journal International, **236**, no. 1, 565–592, doi: 10.1093/gji/ggad424.

Gao, K., and T. Chen, 2024, FLIT: A generic Fortran library based on interfaces and templates: GitHub Open-source Repository, doi: github.com/lanl/flit.

Gao, K., C. Donahue, B. G. Henderson, and R. T. Modrak, 2022, Deep-learning-guided high-resolution subsurface reflectivity imaging with application to ground-penetrating radar data: Geophysical Journal International, **233**, no. 1, 448–471, doi: 10.1093/gji/ggac468.

Gao, K., and L. Huang, 2019, Acoustic- and elastic-waveform inversion with total generalized p-variation regularization: Geophysical Journal International, **218**, no. 2, 933–957, doi: 10.1093/gji/ggz203.

Gauthier, O., J. Virieux, and A. Tarantola, 1986, Two-dimensional nonlinear inversion of seismic waveforms: Numerical results: Geophysics, **51**, no. 7, 1387–1403, doi: 10.1190/1.1442188.

Gibson, R. L., V. Durussel, and K.-J. Lee, 2005, Modeling and velocity analysis with a wavefront-construction algorithm for anisotropic media: Geophysics, **70**, no. 4, T63–T74, doi: 10.1190/1.1988188.

Goldstein, T., and S. Osher, 2009, The split Bregman method for L1-regularized problems: SIAM Journal on Imaging Sciences, **2**, no. 2, 323–343, doi: 10.1137/080725891.

Grechka, V. Y., and G. A. McMechan, 1996, 3-D two-point ray tracing for heterogeneous, weakly transversely isotropic media: Geophysics, **61**, no. 6, 1883–1894, doi: 10.1190/1.1444103.

Guitton, A., 2012, Blocky regularization schemes for full-waveform inversion: Geophysical Prospecting, **60**, no. 5, 870–884, doi: 10.1111/j.1365-2478.2012.01025.x.

Guo, H., and C. Thurber, 2021, Double-difference seismic attenuation tomography method and its application to The Geysers geothermal field, California: Geophysical Journal International, **225**, no. 2, 926–949, doi: 10.1093/gji/ggab017.

Huang, J.-W., and G. Bellefleur, 2012, Joint transmission and reflection traveltime tomography using the fast sweeping method and the adjoint-state technique: Geophysical Journal International, **188**, no. 2, 570–582, doi: 10.1111/j.1365-246X.2011.05273.x.

Kao, C. Y., S. Osher, and J. Qian, 2004, Lax-Friedrichs sweeping scheme for static Hamilton-Jacobi equations: Journal of Computational Physics, **196**, no. 1, 367 – 391, doi: https://doi.org/10.1016/j.jcp.2003.11.007.

Kao, C.-Y., S. Osher, and Y.-H. Tsai, 2005, Fast Sweeping Methods for Static Hamilton–Jacobi Equations: SIAM Journal on Numerical Analysis, **42**, no. 6, 2612–2632, doi: 10.1137/S0036142902419600.

Kim, S., 2002, 3-D eikonal solvers: First-arrival traveltimes: Geophysics, **67**, no. 4, 1225–1231, doi: 10.1190/1.1500384.

Kim, S., and R. Cook, 1999, 3-d traveltime computation using second-order eno scheme: Geophysics, **64**, no. 6, 1867–1876, doi: 10.1190/1.1444693.

Knoll, F., K. Bredies, T. Pock, and R. Stollberger, 2011, Second order total generalized variation (TGV) for MRI: Magnetic Resonance in Medicine, **65**, no. 2, 480–491, doi: 10.1002/mrm.22595.

Koehn, D., and D. De Nil, 2022, RAJZEL – 2D parallel first-arrival traveltime modelling and inversion code using an Eikonal solver and the adjoint state method: GitHub Repository, doi: github.com/daniel-koehn/RAJZEL.

Korenaga, J., W. S. Holbrook, G. M. Kent, P. B. Kelemen, R. S. Detrick, H. Larsen, J. R. Hopper, and T. Dahl-Jensen, 2000, Crustal structure of the southeast Greenland margin from joint refraction and reflection seismic tomography: Journal of Geophysical Research: Solid Earth, **105**, no. B9, 21591–21614, doi: 10.1029/2000JB900188.

Lambaré, G., P. S. Lucio, and A. Hanyga, 1996, Two-dimensional multivalued traveltime and amplitude maps by uniform sampling of a ray field: Geophysical Journal International, **125**, no. 2, 584–598, doi: 10.1111/j.1365-246X.1996.tb00021.x.

Le Bouteiller, P., M. Benjemaa, L. Métivier, and J. Virieux, 2019, A discontinuous Galerkin fast-sweeping eikonal solver for fast and accurate traveltime computation in 3D tilted anisotropic media: Geophysics, **84**, no. 2, C107–C118, doi: 10.1190/geo2018-0555.1.

Leung, S., and J. Qian, 2006, An adjoint state method for three-dimensional transmission traveltime tomography using first-arrivals: Communications in Mathematical Sciences, **4**, no. 1, 249–266.

Li, Y., L. Dong, and Y. Liu, 2017, First-arrival traveltime tomography based on a new preconditioned adjoint-state method: Chinese Journal of Geophysics, **228**, no. 10, 3934–3941, doi: 10.6038/cjg20171021.

Lin, Y., and L. Huang, 2014, Acoustic- and elastic-waveform inversion using a modified total-variation regularization scheme: Geophysical Journal International, **200**, no. 1, 489–502, doi: 10.1093/gji/ggu393.

Lin, Y., E. M. Syracuse, M. Maceira, H. Zhang, and C. Larmat, 2015, Double-difference traveltime tomography with edge-preserving regularization and a priori interfaces: Geophysical Journal International, **201**, no. 2, 574–594, doi: 10.1093/gji/ggv047.

Liu, Q., and J. Tromp, 2006, Finite-frequency kernels based on adjoint methods: Bulletin of the Seismological Society of America, **96**, no. 6, 2383–2397, doi: 10.1785/0120060041.

Liu, Y., L. Dong, Y. Wang, J. Zhu, and Z. Ma, 2009, Sensitivity kernels for seismic Fresnel volume tomography: Geophysics, **74**, no. 5, U35–U46, doi: 10.1190/1.3169600.

Luo, S., and J. Qian, 2011, Factored singularities and high-order Lax-Friedrichs sweeping schemes for point-source traveltimes and amplitudes: Journal of Computational Physics, **230**, no. 12, 4742–4755, doi: 10.1016/j.jcp.2011.02.043.

———, 2012, Fast sweeping methods for factored anisotropic eikonal equations: Multiplicative and additive factors: Journal of Scientific Computing, **52**, no. 2, 360–382, doi: 10.1007/s10915-011-9550-y.

Luo, S., J. Qian, and H. Zhao, 2012, Higher-order schemes for 3D first-arrival traveltimes and amplitudes: Geophysics, **77**, no. 2, T47–T56, doi: 10.1190/geo2010-0363.1.

Luo, Y., Y. Ma, Y. Wu, H. Liu, and L. Cao, 2016, Full-traveltime inversion: Geophysics, **81**, no. 5, R261–R274, doi: 10.1190/geo2015-0353.1.

Luo, Y., and G. T. Schuster, 1991, Wave-equation traveltime inversion: Geophysics, **56**, no. 5, 645–653, doi: 10.1190/1.1443081.

Marquering, H., F. Dahlen, and G. Nolet, 1999, Three-dimensional sensitivity kernels for finite-frequency traveltimes: the banana–doughnut paradox: Geophysical Journal International, **137**, no. 3, 805–815, doi: 10.1046/j.1365-246x.1999.00837.x.

Meléndez, A., J. Korenaga, V. Sallarès, A. Miniussi, and C. Ranero, 2015, TOMO3D: 3-D joint refraction and reflection traveltime tomography parallel code for active-source seismic data—synthetic test: Geophysical Journal International, **203**, no. 1, 158–174, doi: 10.1093/gji/ggv292.

Michelena, R. J., and J. M. Harris, 1991, Tomographic traveltime inversion using natural pixels: Geophysics, **56**, no. 5, 635–644, doi: 10.1190/1.1443080.

Mora, P., 1987, Nonlinear two-dimensional elastic inversion of multioffset seismic data: Geophysics, **52**, no. 9, 1211–1228, doi: 10.1190/1.1442384.

Nocedal, J., and S. J. Wright, 2006, Numerical Optimization (2nd ed.): Springer, New York.

Pereyra, V., W. H. K. Lee, and H. B. Keller, 1980, Solving two-point seismic-ray tracing problems in a heterogeneous medium: Part 1. A general adaptive finite difference method: Bulletin of the Seismological Society of America, **70**, no. 1, 79–99.

Plessix, R.-E., 2006, A review of the adjoint-state method for computing the gradient of a functional with geophysical applications: Geophysical Journal International, **167**, no. 2, 495–503, doi: 10.1111/j.1365-246X.2006.02978.x.

Podvin, P., and I. Lecomte, 1991, Finite difference computation of traveltimes in very contrasted velocity models: a massively parallel approach and its associated tools: Geophysical Journal International, **105**, no. 1, 271–284, doi: 10.1111/j.1365-246X.1991.tb03461.x.

Pyun, S., C. Shin, D.-J. Min, and T. Ha, 2005, Refraction traveltime tomography using damped monochromatic wavefield: Geophysics, **70**, no. 2, U1–U7, doi: 10.1190/1.1884829.

Qian, J., and W. W. Symes, 2002, Finite-difference quasi-P traveltimes for anisotropic media: Geophysics, **67**, no. 1, 147–155, doi: 10.1190/1.1451438.

Qian, J., Y.-T. Zhang, and H.-K. Zhao, 2007, Fast sweeping methods for eikonal equations on triangular meshes: SIAM J. Numer. Anal., **45**, no. 1, 83–107, doi: 10.1137/050627083.

Qin, F., Y. Luo, K. B. Olsen, W. Cai, and G. T. Schuster, 1992, Finite-difference solution of the eikonal equation along expanding wavefronts: Geophysics, **57**, no. 3, 478–487, doi: 10.1190/1.1443263.

Rawlinson, N., M. d. Kool, and M. Sambridge, 2006, Seismic wavefront tracking in 3D heterogeneous media: Applications with multiple data classes: Exploration Geophysics, **37**, no. 4, 322–330, doi: 10.1071/EG06322.

Rawlinson, N., S. Pozgay, and S. Fishwick, 2010, Seismic tomography: A window into deep Earth: Physics of the Earth and Planetary Interiors, **178**, no. 3, 101–135, doi: 10.1016/j.pepi.2009.10.002.

Rawlinson, N., and M. Sambridge, 2004, Wave front evolution in strongly heterogeneous layered media using the fast marching method: Geophysical Journal International, **156**, no. 3, 631–647, doi: 10.1111/j.1365-246X.2004.02153.x.

Rudin, L. I., S. Osher, and E. Fatemi, 1992, Nonlinear total variation based noise removal algorithms: Physica D: Nonlinear Phenomena, **60**, no. 1, 259 – 268, doi: 10.1016/0167-2789(92)90242-F.

Sadeghi, H., S. Suzuki, and H. Takenaka, 1999, A two-point, three-dimensional seismic ray tracing using genetic algorithms: Physics of the Earth and Planetary Interiors, **113**, no. 1, 355 – 365, doi: 10.1016/S0031-9201(99)00011-4.

Schuster, G. T., and A. Quintus-Bosz, 1993, Wavepath eikonal traveltime inversion: Theory: Geophysics, **58**, no. 9, 1314–1323, doi: 10.1190/1.1443514.

Sei, A., and W. W. Symes, 1994, Gradient calculation of the traveltime cost function without ray tracing: SEG Technical Program Expanded Abstracts, 1351–1354, doi: 10.1190/1.1822780.

Sethian, J. A., and A. M. Popovici, 1999, 3-D traveltime computation using the fast marching method: Geophysics, **64**, no. 2, 516–523, doi: 10.1190/1.1444558.

Snieder, R., and A. Lomax, 1996, Wavefield smoothing and the effect of rough velocity perturbations on arrival times and amplitudes: Geophysical Journal International, **125**, no. 3, 796–812, doi: 10.1111/j.1365-246X.1996.tb06024.x.

Spetzler, J., and R. Snieder, 2004, The Fresnel volume and transmitted waves: Geophysics, **69**, no. 3, 653–663, doi: 10.1190/1.1759451.

Taillandier, C., M. Noble, H. Chauris, and H. Calandra, 2009, First-arrival traveltime tomography based on the adjoint-state method: Geophysics, **74**, no. 6, WCB1–WCB10, doi: 10.1190/1.3250266.

Tarantola, A., 1984, Inversion of seismic reflection data in the acoustic approximation: Geophysics, **49**, no. 8, 1259–1266, doi: 10.1190/1.1441754.

Thurber, C. H., 1983, Earthquake locations and three-dimensional crustal structure in the Coyote Lake Area, central California: Journal of Geophysical Research: Solid Earth, **88**, no. B10, 8226–8236, doi: 10.1029/JB088iB10p08226.

Tikhonov, A., A. Goncharsky, V. Stepanov, and A. Yagola, 1995, Numerical methods for the solution of ill-posed problems: Springer.

Tong, P., 2021a, Adjoint-state traveltime tomography: Eikonal equation-based methods and application to the Anza Area in Southern California: Journal of Geophysical Research: Solid Earth, **126**, no. 5, e2021JB021818, doi: 10.1029/2021JB021818.

———, 2021b, Adjoint-state traveltime tomography software package (Training version): GitHub Repository, doi: doi.org/10.21979/N9/YPGQRF.

Tong, P., T. Li, J. Chen, and M. Nagaso, 2024, Adjoint-state differential arrival time tomography: Geophysical Journal International, **236**, no. 1, 139–160, doi: 10.1093/gji/ggad416.

Tong, P., D. Yang, Q. Liu, X. Yang, and J. Harris, 2016, Acoustic wave-equation-based earthquake location: Geophysical Journal International, **205**, no. 1, 464–478, doi: 10.1093/gji/ggw026.

Tsai, Y., L. Cheng, S. Osher, and H. Zhao, 2003, Fast sweeping algorithms for a class of Hamilton-Jacobi equations: SIAM Journal on Numerical Analysis, **41**, no. 2, 673–694, doi: 10.1137/S0036142901396533.

Vasco, D. W., J. John E. Peterson, and E. L. Majer, 1995, Beyond ray tomography: Wavepaths and Fresnel volumes: Geophysics, **60**, no. 6, 1790–1804, doi: 10.1190/1.1443912.

Vidale, J., 1988, Finite-difference calculation of travel times: Bulletin of the Seismological Society of America, **78**, no. 6, 2062–2076.

Vinje, V., E. Iversen, and H. Gjøystdal, 1993, Traveltime and amplitude estimation using wavefront construction: Geophysics, **58**, no. 8, 1157–1166, doi: 10.1190/1.1443499.

Virieux, J., and S. Operto, 2009, An overview of full-waveform inversion in exploration geophysics: Geophysics, **74**, no. 6, WCC1–WCC26, doi: 10.1190/1.3238367.

Waheed, U. B., and T. Alkhalifah, 2017, A fast sweeping algorithm for accurate solution of the tilted transversely isotropic eikonal equation using factorization: Geophysics, **82**, no. 6, WB1–WB8, doi: 10.1190/geo2016-0712.1.

Waheed, U. B., T. Alkhalifah, and H. Wang, 2015a, Efficient traveltime solutions of the acoustic TI eikonal equation: Journal of Computational Physics, **282**, 62 – 76, doi: 10.1016/j.jcp.2014.11.006.

Waheed, U. B., C. E. Yarman, and G. Flagg, 2015b, An iterative, fast-sweeping-based eikonal solver for 3D tilted anisotropic media: Geophysics, **80**, no. 3, C49–C58, doi: 10.1190/geo2014-0375.1.

Waldhauser, F., and W. L. Ellsworth, 2000, A double-difference earthquake location algorithm: Method and application to the Northern Hayward Fault, California: Bulletin of the Seismological

Society of America, **90**, no. 6, 1353–1368, doi: 10.1785/0120000006.
Wang, Y., T. Nemeth, and R. T. Langan, 2006, An expanding-wavefront method for solving the eikonal equations in general anisotropic media: Geophysics, **71**, no. 5, T129–T135, doi: 10.1190/1.2235563.
White, M. C. A., H. Fang, N. Nakata, and Y. Ben-Zion, 2020, PyKonal: A Python package for solving the eikonal equation in spherical and Cartesian coordinates using the fast marching method: Seismological Research Letters, **91**, no. 4, 2378–2389, doi: 10.1785/0220190318.
Woodward, M. J., 1992, Wave-equation tomography: Geophysics, **57**, no. 1, 15–26, doi: 10.1190/1.1443179.
Wu, R., and M. N. Toksöz, 1987, Diffraction tomography and multisource holography applied to seismic imaging: Geophysics, **52**, no. 1, 11–25, doi: 10.1190/1.1442237.
Wu, X., and Z. Guo, 2018, Detecting faults and channels while enhancing seismic structural and stratigraphic features: Interpretation, **7**, no. 1, T155–T166, doi: 10.1190/INT-2017-0174.1.
Xu, S., Y. Zhang, and T. Huang, 2006, Enhanced tomography resolution by a fat ray technique: SEG Technical Program Expanded Abstracts 2006, 3354–3358, doi: 10.1190/1.2370229.
Yomogida, K., 1992, Fresnel zone inversion for lateral heterogeneities in the earth: Pure and Applied Geophysics, **138**, no. 3, 391–406, doi: 10.1007/BF00876879.
Yuan, Y. O., F. J. Simons, and J. Tromp, 2016, Double-difference adjoint seismic tomography: Geophysical Journal International, **206**, no. 3, 1599–1618, doi: 10.1093/gji/ggw233.
Zelt, C. A., and P. J. Barton, 1998, Three-dimensional seismic refraction tomography: A comparison of two methods applied to data from the Faeroe Basin: Journal of Geophysical Research: Solid Earth, **103**, no. B4, 7187–7210, doi: 10.1029/97JB03536.
Zelt, C. A., and J. Chen, 2016, Frequency-dependent traveltime tomography for near-surface seismic refraction data: Geophysical Journal International, **207**, no. 1, 72–88, doi: 10.1093/gji/ggw269.
Zeng, X., C. H. Thurber, D. R. Shelly, R. M. Harrington, E. S. Cochran, N. L. Bennington, D. Peterson, B. Guo, and K. McClement, 2016, 3-D P- and S-wave velocity structure and low-frequency earthquake locations in the Parkfield, California region: Geophysical Journal International, **206**, no. 3, 1574–1585, doi: 10.1093/gji/ggw217.
Zhang, H., and C. Thurber, 2006, Development and applications of double-difference seismic tomography: pure and applied geophysics, **163**, no. 2, 373–403, doi: 10.1007/s00024-005-0021-y.
Zhang, H., and C. H. Thurber, 2003, Double-difference tomography: The method and its application to the Hayward Fault, California: Bulletin of the Seismological Society of America, **93**, no. 5, 1875–1889, doi: 10.1785/0120020190.

Zhang, J., L. Dong, J. Wang, and C. Huang, 2023, Preconditioned transmission + reflection joint traveltime tomography with adjoint-state method for subsurface velocity model building: Geophysical Prospecting, **71**, no. 2, 171–190, doi: 10.1111/1365-2478.13287.

Zhang, J., U. S. ten Brink, and M. N. Toksöz, 1998, Nonlinear refraction and reflection travel time tomography: Journal of Geophysical Research: Solid Earth, **103**, no. B12, 29743–29757, doi: 10.1029/98JB01981.

Zhang, J., and M. N. Toksöz, 1998, Nonlinear refraction traveltime tomography: Geophysics, **63**, no. 5, 1726–1737, doi: 10.1190/1.1444468.

Zhang, Y.-T., H.-K. Zhao, and J. Qian, 2006, High order fast sweeping methods for static Hamilton-Jacobi equations: Journal of Scientific Computing, **29**, no. 1, 25–56, doi: 10.1007/s10915-005-9014-3.

Zhao, H., 2004, A fast sweeping method for eikonal equations: Mathematics of Computation, **74**, no. 250, 603–627, doi: 10.1090/S0025-5718-04-01678-3.

Zhdanov, M., 2002, Geophysical inverse theory and regularization problems, 1 ed.: Elsevier Science.

Appendix A: Parallel fast sweeping algorithms for the eikonal and adjoint-state equations

We slightly modify the parallel fast sweeping algorithm presented in Detrixhe et al. (2013). For the purpose of completeness, we detail our algorithms as below.

Fast sweeping relies on sweeping all possible orders of dimension directions. For 2D, the possible ordering of directions are

$$I = 1 : N_x, \quad K = 1 : N_z, \tag{56a}$$
$$I = 1 : N_x, \quad K = N_z : 1, \tag{56b}$$
$$I = N_x : 1, \quad K = 1 : N_z, \tag{56c}$$
$$I = N_x : 1, \quad K = N_z : 1. \tag{56d}$$

We denote each of the orderings as $S(x_0, x_1, z_0, z_1)$, where we use subscripts 0 and 1 to represent the starting and end elements, respectively. For example, for the second ordering, $(x_0, x_1, z_0, z_1) = (1, N_x, N_z, 1)$.

Then we implement the parallel fast sweeping in 2D for a specific ordering $S(x_0, x_1, z_0, z_1)$ with Algorithm 1.

Algorithm 1: Algorithm for 2D parallel fast sweeping adopted and modified from Detrixhe et al. (2013) for LATTE.

Input: Velocity model, traveltime field τ or adjoint-state field λ

Parameters: Ordering $S(x_0, x_1, z_0, z_1)$, dimensions of the model N_x and N_z, and grid spacings d_x and d_z

for $1 \leq l \leq N_x + N_z - 1$ **do**

Compute the starting and ending element indices for z dimension as:

$$j_a = \begin{cases} j_0, & l \leq N_x \\ j_0 + (l - N_x) \times c_j, & \text{otherwise.} \end{cases} \tag{57}$$

$$j_b = \begin{cases} j_0 + (l - 1) \times c_j, & l \leq N_z \\ j_1, & \text{otherwise,} \end{cases} \tag{58}$$

where

$$c_j = \begin{cases} 1, & \text{if } j_0 \leq j_1, \\ -1, & \text{otherwise.} \end{cases} \tag{59}$$

for parallel $j_a \leq j \leq j_b$ **do**

(1) Compute x index i from

$$|i - i_0| + |j - j_0| = l - 1. \tag{60}$$

(2) Update the multiplicative traveltime field $\tau_{i,j}$ or the adjoint-state field $\lambda_{i,j}$.

end

end

Output: τ or λ

For 3D, the possible ordering of directions are

$$I = 1 : N_x, \quad J = 1 : N_y, \quad K = 1 : N_z, \tag{61a}$$

$$I = 1 : N_x, \quad J = 1 : N_y, \quad K = N_z : 1, \tag{61b}$$

$$I = 1 : N_x, \quad J = N_y : 1, \quad K = 1 : N_z, \tag{61c}$$

$$I = 1 : N_x, \quad J = N_y : 1, \quad K = N_z : 1, \tag{61d}$$

$$I = N_x : 1, \quad J = 1 : N_y, \quad K = 1 : N_z, \tag{61e}$$

$$I = N_x : 1, \quad J = 1 : N_y, \quad K = N_z : 1, \tag{61f}$$

$$I = N_x : 1, \quad J = N_y : 1, \quad K = 1 : N_z, \tag{61g}$$

$$I = N_x : 1, \quad J = N_y : 1, \quad K = N_z : 1. \tag{61h}$$

We denote each of the orderings as $S(x_0, x_1, y_0, y_1, z_0, z_1)$, where we use subscripts 0 and 1 to represent the starting and end elements, respectively. For example, for the second ordering, $(x_0, x_1, y_0, y_1, z_0, z_1) = (1, N_x, 1, N_y, N_z, 1)$.

The algorithm for 3D parallel fast sweeping is not straightforwardly available from Detrixhe et al. (2013). Therefore, here we provide a complete algorithm for achieving parallel fast sweeping with an arbitrary number of threads for 3D eikonal and adjoint-state equations. We implement 3D parallel fast sweeping for a specific ordering $S(x_0, x_1, y_0, y_1, z_0, z_1)$ with Algorithm 2.

Then we go to the next ordering and repeat the procedure until all orderings are computed. We repeat the entire procedure (fast sweeping of 4 orderings in 2D and 8 orderings in 3D) until the threshold of field difference is reached. Here we ignore the outer loop algorithm as the details have been described by a number of existing works (e.g., Zhao, 2004; Taillandier et al., 2009; Detrixhe et al., 2013). The algorithm has the same computational complexity with serial fast sweeping yet can be accelerated with OpenMP shared-memory parallelism.

Appendix B: The adjoint-state equation for arbitrary receiver location

In the original works of adjoint-state FATT by Leung and Qian (2006) and later by Taillandier et al. (2009), the authors developed the formulation for adjoint-state equation. However, in both works, solving the adjoint-state equation requires the determination of the adjoint-state variable λ on the boundaries through

$$\lambda(\mathbf{x}_r)\nabla t(\mathbf{x}_r) \cdot \mathbf{n}(\mathbf{x}_r) = \Delta T(\mathbf{x}_r), \tag{69}$$

where $\mathbf{n}$ is the normal to the surface (or boundary) of the model, $\partial\Omega$. This condition introduces nontrivial restriction on the applicability of adjoint-state FATT to arbitrary source-receiver geometry in a rigorous sense. For instance, rigorously, adjoint-state FATT does not apply to the scenario where the receivers are placed in a well or below the ground surface.

We argue that such a restriction is not necessary. The emergence of this condition is in fact caused by the assumption that the receivers are placed on the surface $\partial\Omega$. Rather than defining the misfit function using the surface integral of the traveltime misfit on $\partial\Omega$, we assume the following constrained L_2-norm optimization problem:

$$\mathcal{J}(m) = \min_m \frac{1}{2} \int_\Omega [t(m, \mathbf{x}) - T(\mathbf{x})]^2 \, \delta(\mathbf{x} - \mathbf{x}_r) d\mathbf{x}, \quad \text{s.t.} \quad m^2 |\nabla t|^2 = 1, \tag{70}$$

where the receivers can be in arbitrary location in Ω.

Algorithm 2: Algorithm for 3D parallel fast sweeping adopted and modified from Detrixhe et al. (2013) for LATTE.

Input: Velocity model, traveltime field τ or adjoint-state field λ

Parameters: Ordering $S(x_0, x_1, y_0, y_1, z_0, z_1)$, dimensions of the model N_x, N_y, and N_z, and grid spacings d_x, d_y, and d_z

for $1 \leq l \leq N_x + N_y + N_z - 2$ **do**

Compute the starting and ending element indices for z and y dimensions as:

$$k_a = \begin{cases} k_0, & l \leq N_x + N_y \\ k_0 + (l - (N_x + N_y - 1)) \times c_k, & \text{otherwise.} \end{cases} \tag{62}$$

$$k_b = \begin{cases} k_0 + (l - 1) \times c_k, & l \leq N_z \\ k_1, & \text{otherwise.} \end{cases} \tag{63}$$

$$j_a = \begin{cases} j_0, & l \leq N_x + N_y \\ j_0 + (l - (N_x + N_y - 1)) \times c_j, & \text{otherwise.} \end{cases} \tag{64}$$

$$j_b = \begin{cases} j_0 + (l - 1) \times c_j, & l \leq N_y \\ j_1, & \text{otherwise,} \end{cases} \tag{65}$$

where

$$c_k = \begin{cases} 1, & \text{if } k_0 \leq k_1, \\ -1, & \text{otherwise,} \end{cases}, \tag{66}$$

$$c_j = \begin{cases} 1, & \text{if } j_0 \leq j_1, \\ -1, & \text{otherwise.} \end{cases} \tag{67}$$

for parallel $k_a \leq k \leq k_b,\ j_a \leq j \leq j_b$ **do**

(1) Compute x index i from

$$|i - i_0| + |j - j_0| + |k - k_0| = l - 1. \tag{68}$$

(2) If $i < 1$ or $i > N_x$, then skip Step (3).

(3) Update the multiplicative traveltime field $\tau_{i,j,k}$ or the adjoint-state field $\lambda_{i,j,k}$.

end

end

Output: τ or λ

Defining the augmented Lagrangian,

$$\mathcal{L}(m, t, \lambda) = \frac{1}{2} \int_\Omega (t - T)^2 \delta(\mathbf{x} - \mathbf{x}_r) d\mathbf{x} + \frac{1}{2} \int_\Omega \lambda \left(|\nabla t|^2 - \frac{1}{m^2} \right) d\mathbf{x}, \tag{71}$$

the first-order optimality conditions (Nocedal and Wright, 2006) of which read

$$
\begin{aligned}
\frac{\partial \mathcal{L}}{\partial m} &= \frac{\partial \mathcal{J}}{\partial m} + \int_{\Omega} \frac{\lambda}{m^3} d\mathbf{x} = 0, && (72)\\
\frac{\partial \mathcal{L}}{\partial t} &= 0, && (73)\\
\frac{\partial \mathcal{L}}{\partial \lambda} &= |\nabla t|^2 - \frac{1}{m^2} = 0. && (74)
\end{aligned}
$$

The second equation, $\partial \mathcal{L}/\partial t = 0$, gives

$$
\begin{aligned}
\frac{\partial \mathcal{L}}{\partial t} &= \int_{\Omega} (t-T)\delta(\mathbf{x}-\mathbf{x}_r) d\mathbf{x} + \int_{\Omega} \left(\nabla t \cdot \frac{\partial \nabla t}{\partial t} \right) \lambda d\mathbf{x} \\
&= \int_{\Omega} (t-T)\delta(\mathbf{x}-\mathbf{x}_r) d\mathbf{x} + \int_{\Omega} \left[\nabla t \cdot \frac{\partial}{\partial t} \left(\frac{\partial t}{\partial \mathbf{x}} \right) \right] \lambda d\mathbf{x} \\
&= \int_{\Omega} (t-T)\delta(\mathbf{x}-\mathbf{x}_r) d\mathbf{x} + \int_{\Omega} \nabla t \cdot \nabla \lambda d\mathbf{x}. && (75)
\end{aligned}
$$

If we assume $\lambda = 0$ on $\partial\Omega$, then we can add an arbitrary boundary integral term of λ to equation (75). By adding $\int_{\partial\Omega} \lambda(\mathbf{n} \cdot \nabla t) ds$ where $\mathbf{n}$ is the normal vector of $\partial\Omega$ and using integration by parts, we have

$$
\begin{aligned}
\frac{\partial \mathcal{L}}{\partial t} &= \int_{\Omega} (t-T)\delta(\mathbf{x}-\mathbf{x}_r) d\mathbf{x} + \int_{\Omega} \nabla t \cdot \nabla \lambda d\mathbf{x} - \int_{\partial\Omega} \lambda \mathbf{n} \cdot \nabla t ds, \\
&= \int_{\Omega} (t-T)\delta(\mathbf{x}-\mathbf{x}_r) d\mathbf{x} - \int_{\Omega} \nabla \cdot (\lambda \nabla t) d\mathbf{x} \\
&= 0, && (76)
\end{aligned}
$$

which indicates that, for an arbitrary t and traveltime difference $(t-T)\delta(\mathbf{x}-\mathbf{x}_r)$, the following adjoint-state equation must be satisfied:

$$
\nabla \cdot (\lambda \nabla t) = (t-T)\delta(\mathbf{x}-\mathbf{x}_r). \tag{77}
$$

This is developed in the augmented Lagrangian functional framework as in Leung and Qian (2006) and Taillandier et al. (2009), yet is consistent with the results obtained based on a perturbation approach (Tong, 2021a).

In practice, $\mathbf{x}_r$ can contain multiple nonzero values (multiple receivers). Therefore, writing in a clearer way with more informative notations, we need to solve the adjoint-state equation in the form of

$$
\nabla \cdot [\lambda(\mathbf{x}) \nabla t(m, \mathbf{x})] = \sum_{i=1}^{N_r} [t(m, \mathbf{r}_i) - T(\mathbf{r}_i)], \tag{78}
$$

where we use $\mathbf{r}_i$ to indicate the spatial location of the i-th receiver. The traveltime field $t(m, \mathbf{x})$ is the traveltime corresponding to a model m in some inversion iteration, and is precomputed beforehand.

Equation (78) can be solved using exactly the same method as that described in Appendix A of the work by Taillandier et al. (2009). However, the major difference is that an arbitrary number of $\mathbf{x}_r$ can be at any position of Ω. The initial condition for equation (78) is the traveltime difference, $t(m, \mathbf{r}_i) - T(\mathbf{r}_i)$, at the position of each receiver. For double-difference misfit, it is not difficult to obtain that the adjoint-state equation is

$$\nabla \cdot [\lambda(\mathbf{x}) \nabla t(m, \mathbf{x})] = \sum_{i=1}^{N_r} \left(\sum_{j=1}^{N_r} \left[(t(m, \mathbf{r}_i) - t(m, \mathbf{r}_j)) - (T(\mathbf{r}_i) - T(\mathbf{r}_j)) \right] \right). \tag{79}$$

It is straightforward to derive the adjoint-state equations for the elastic case where $m = (v_p, v_s)$. For brevity, we omit the details here.

Appendix C: Multitask machine learning models for inferring and refining fault attributes from a source image

We develop a multitask supervised ML method to infer and refine fault and fault attributes from a source image. We display the architectures of the multitask inference and refinement NNs in Figure 32. The input to the multitask inference NN is a source image computed using equation (52), while the output from this NN includes the fault probability, fault dip, and fault strike (in 2D, fault strike does not apply). In some cases, the fault surfaces estimated by this inference NN can be "noisy" and contain "cheese holes" (Gao, 2024) because of insufficient source density. Using these fault surfaces as a guidance for source relocation may not be optimal. Therefore, the inference results are then transferred to the multitask refinement NN for refinement, and we use the refined fault attributes in LATTE as a fault/fracture constraint for source location.

In both multitask inference and refinement NNs, we use a residual U-Net (ResUNet) as encoders and decoders. We leverage the ResUNet architecture developed in Gao (2024) to achieve a large inception field. The open-source codes associated with the multitask inference and refinement NNs based on a source image, the training strategy, as well as the algorithms and codes for generating training data and labels, are available in the repository of LATTE.

List of Figures

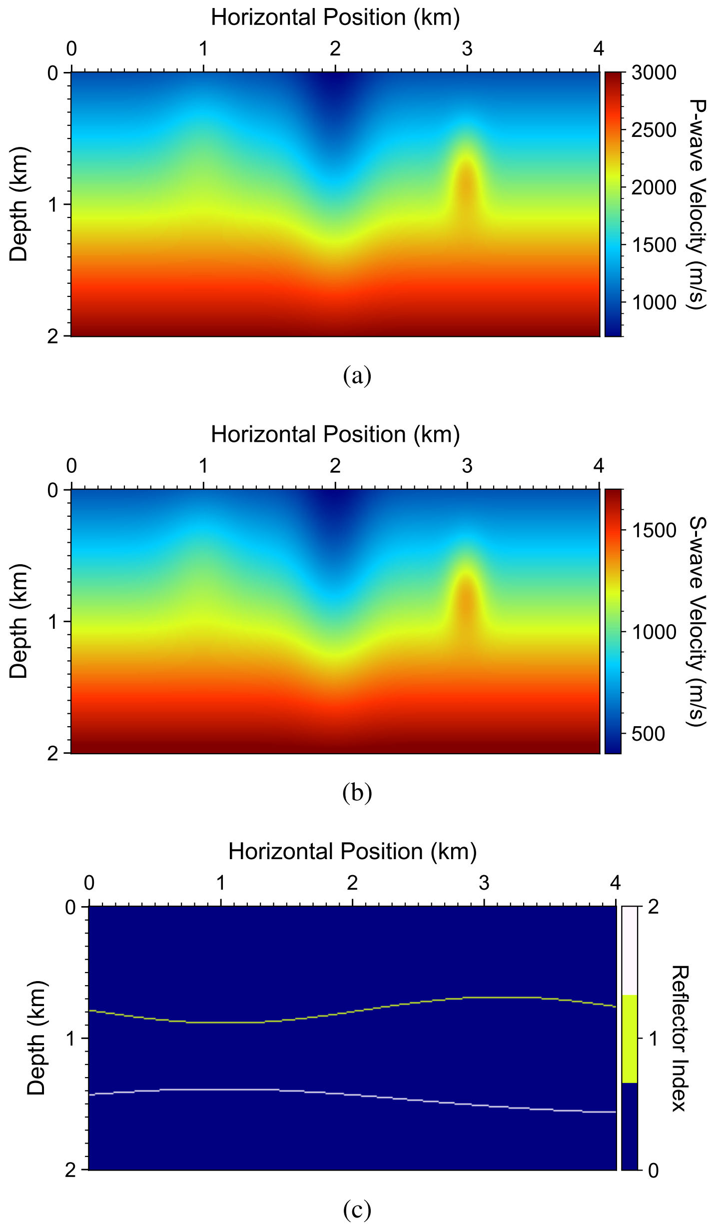

Figure 1: (a) A P-wave velocity model, (b) an S-wave velocity model, and (c) two characteristic reflectors for validating LATTE's traveltime computation functions.

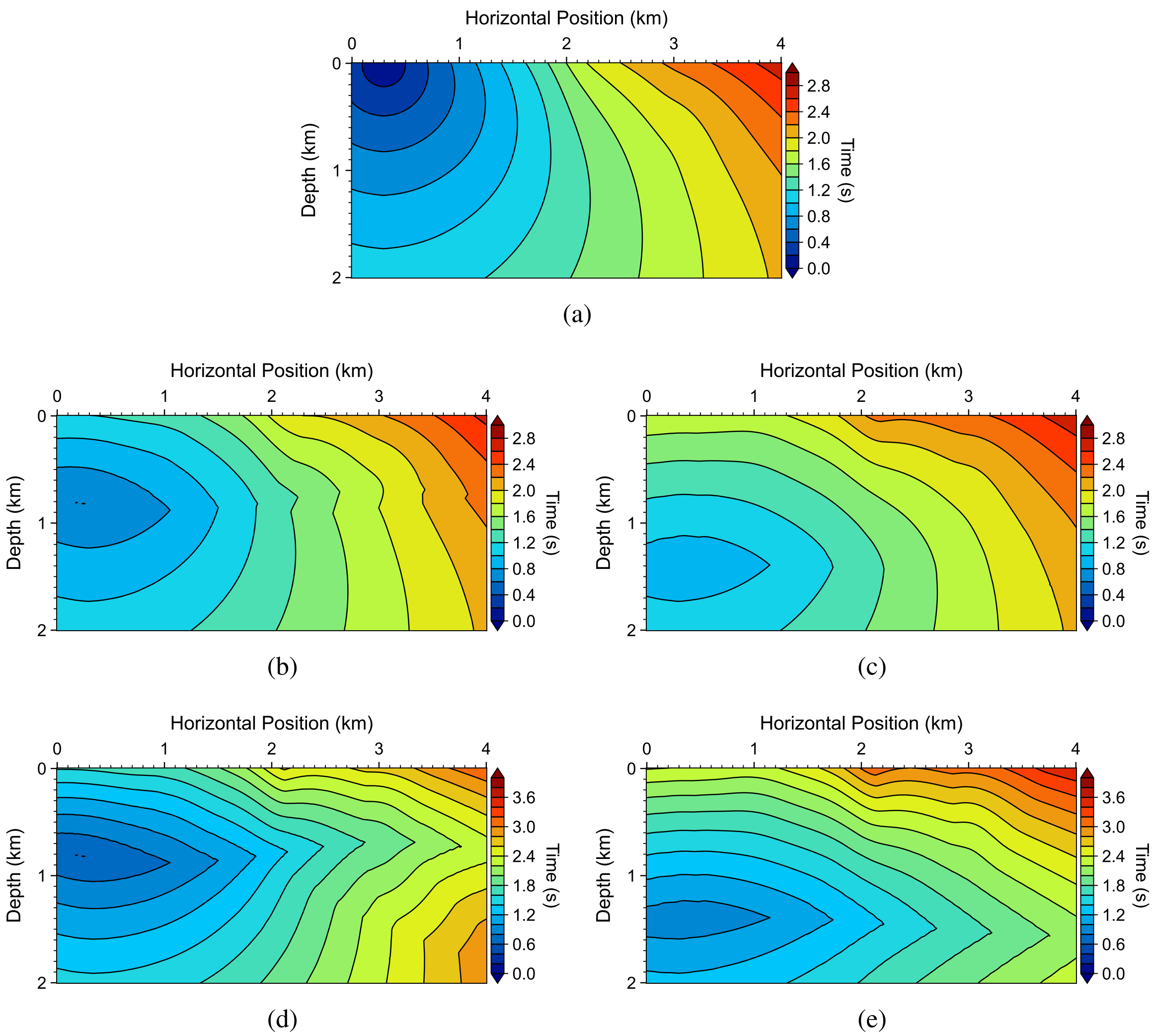

Figure 2: Traveltime fields computed using LATTE eikonal solver for the model shown in Figure 1. (a) First-arrival traveltime field t_p, (b-c) PP-reflection traveltime fields t_{pp}^1 and t_{pp}^2 associated with the first and second reflectors, respectively, and (d-e) PS-reflection traveltime fields t_{ps}^1 and t_{ps}^2 associated with the first and the second reflectors, respectively.

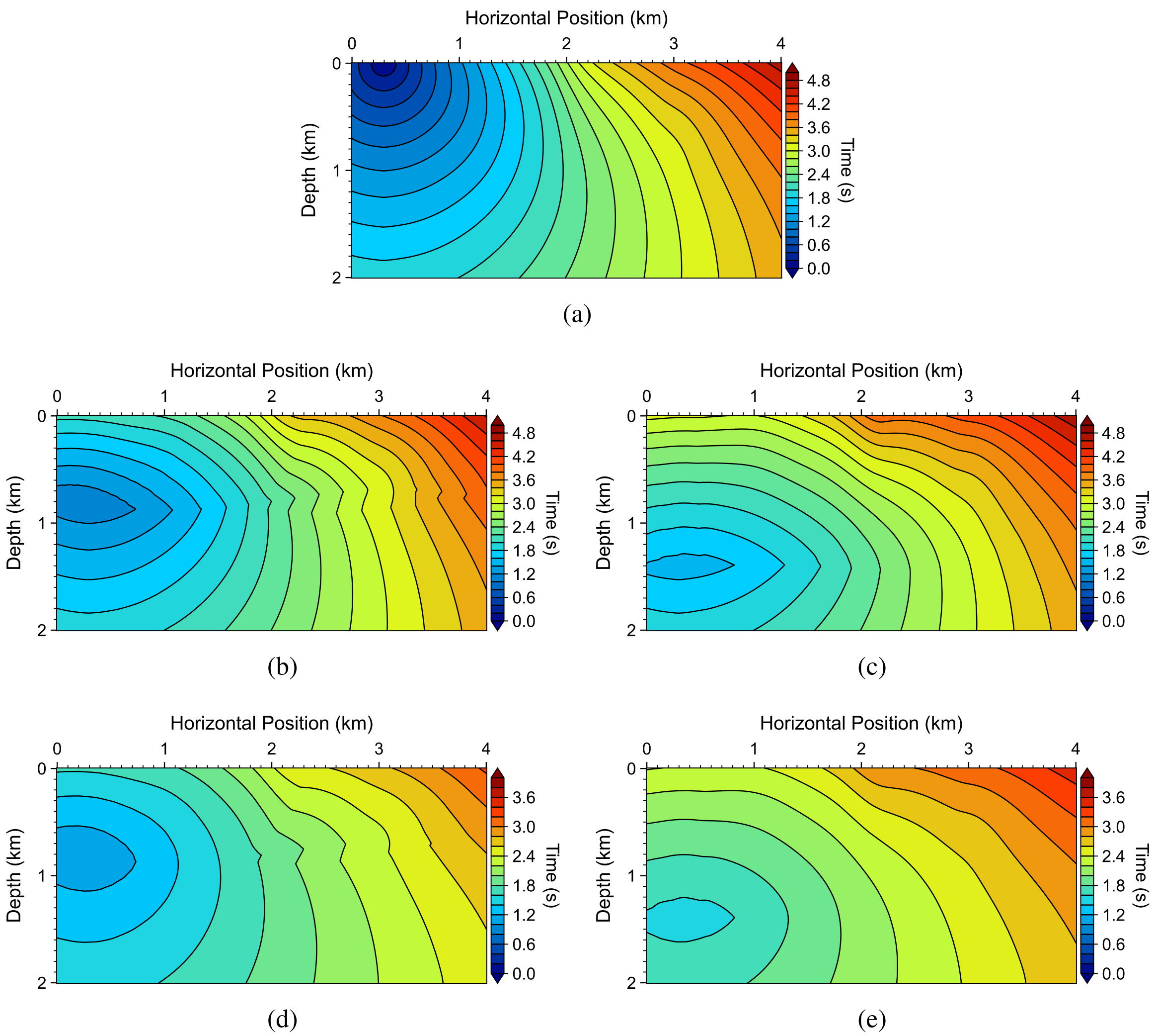

Figure 3: Traveltime fields computed using LATTE eikonal solver for the model shown in Figure 1. (a) First-arrival traveltime field t_s, (b-c) SS-reflection traveltime fields t_{ss}^1 and t_{ss}^2 associated with the first and second reflectors, respectively, and (d-e) SP-reflection traveltime fields t_{sp}^1 and t_{sp}^2 associated with the first and the second reflectors, respectively.

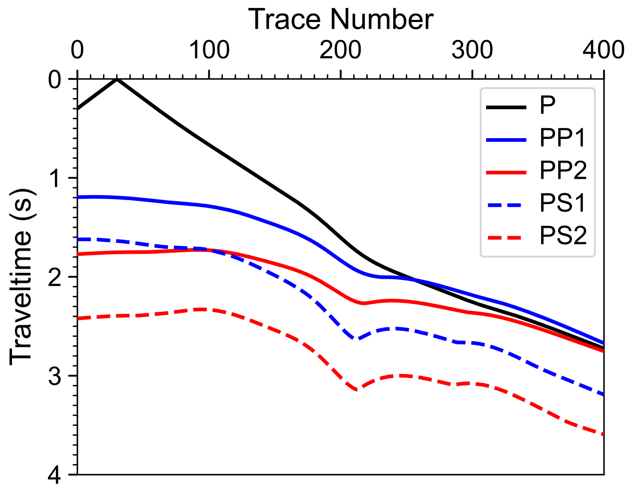

(a)

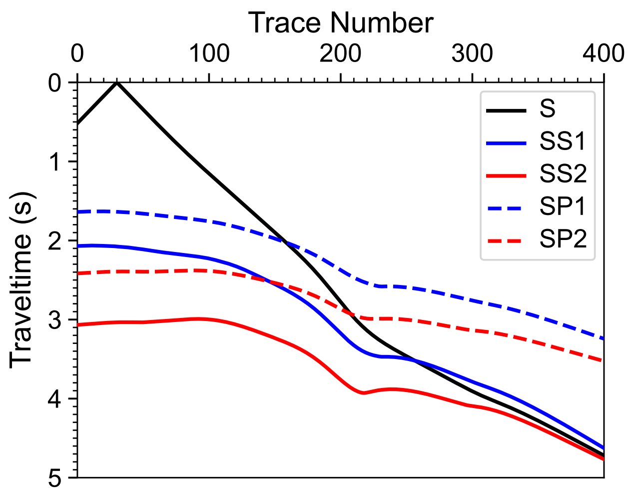

(b)

Figure 4: Traveltime computed using LATTE eikonal solver for (a) P incident wave, and (b) S incident wave, respectively.

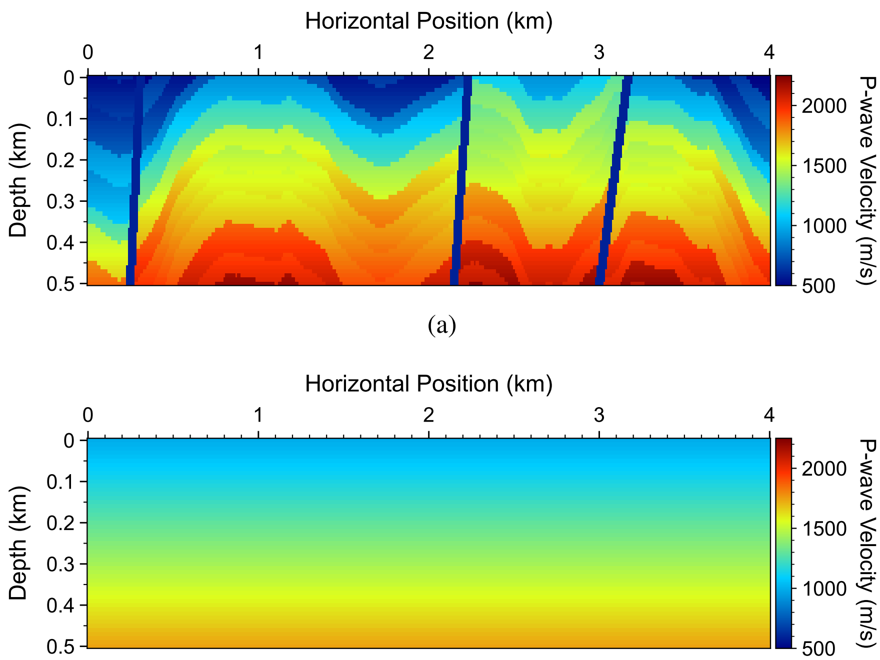

(a)

Horizontal Position (km)

(b)

Figure 5: (a) A v_p model used for validating LATTE's FATT functionality, and (b) smooth 1D v_p as the initial model for FATT.

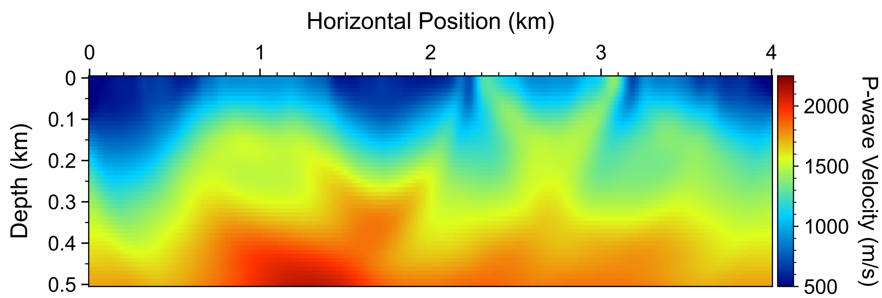

(a)

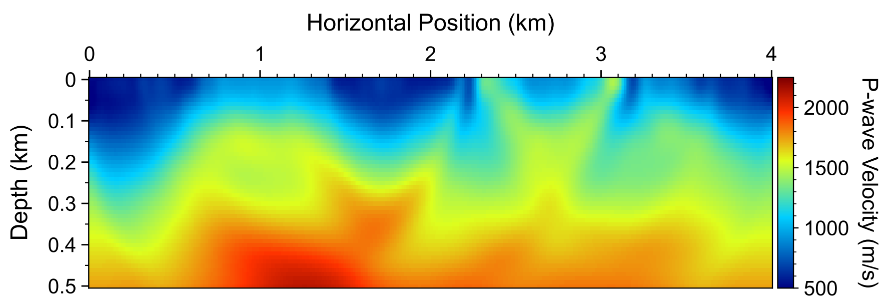

(b)

Figure 6: Inverted v_p models obtained with (a) AD-FATT (absolute traveltime misfit) and (b) DD-FATT (double-difference traveltime misfit), respectively. The results are plotted on the same color scale.

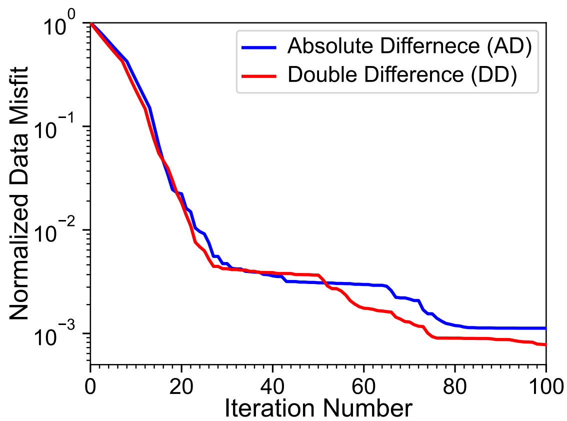

Figure 7: A comparison between the normalized data misfit convergence curves associated with AD-FATT (blue) and DD-FATT (red). The curves are plotted on the logarithmic scale.

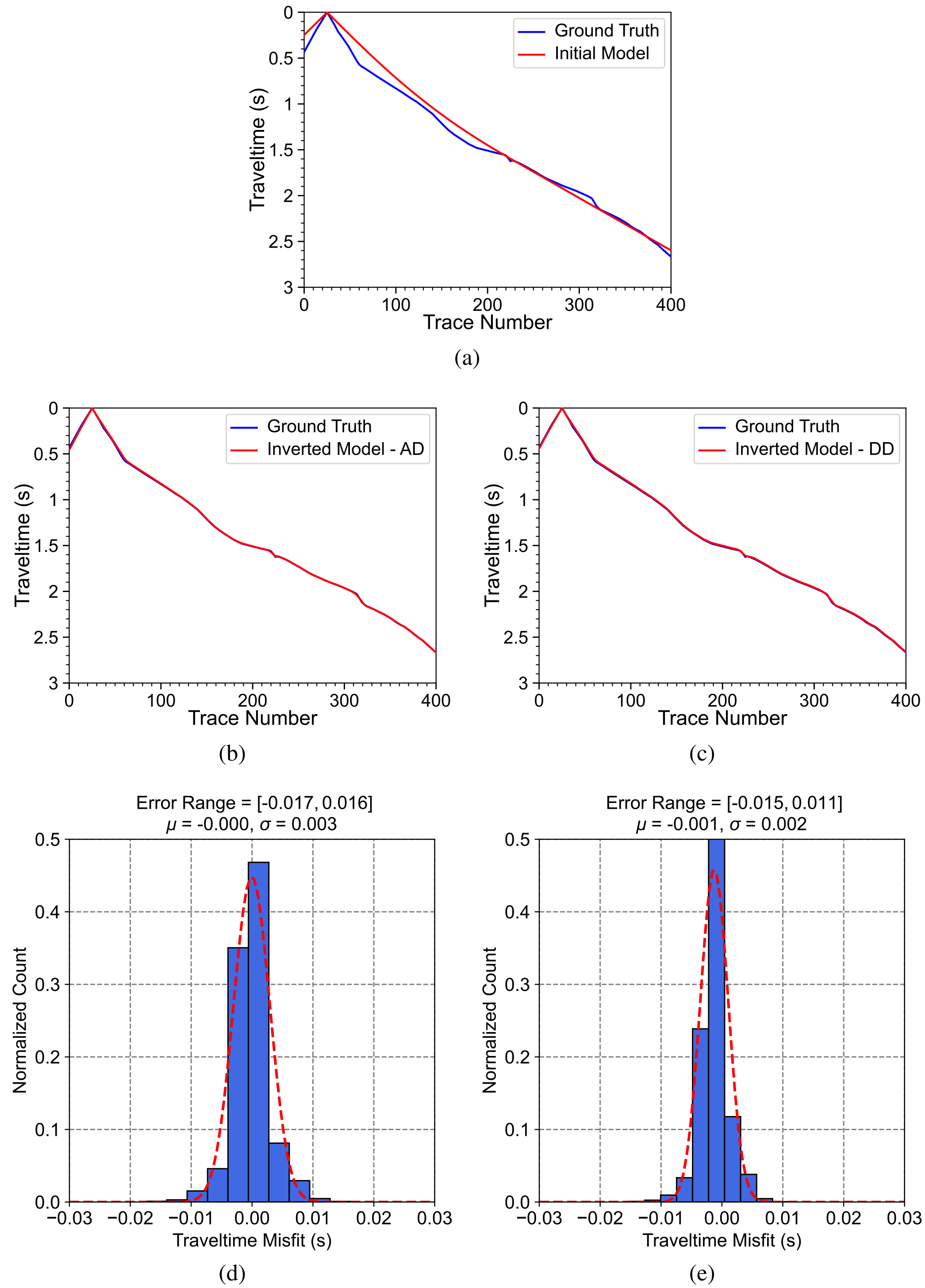

Figure 8: Comparisons between the observed traveltime and the synthetic traveltime of the third source simulated in (a) the initial v_p model, and (b) the AD-FATT-updated v_p model, and (c) DD-FATT-updated v_p model, respectively. Bottom panels display the probability distributions and the fitted Gaussian of traveltime misfit for all the $N_s \times N_r = 40 \times 401$ traces obtained using (d) AD-FATT and (e) DD-FATT, respectively, where a smaller absolute value of μ, a smaller σ, and a narrower error range represent more accurate traveltime fit.

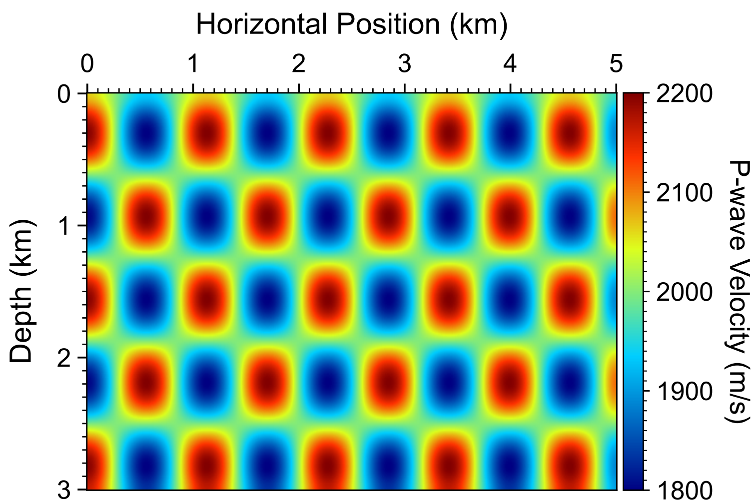

Figure 9: A checkerboard model for validating the source location and joint tomography-location functionalities of LATTE. We set $V_s = V_p/\sqrt{3}$ for simplicity.

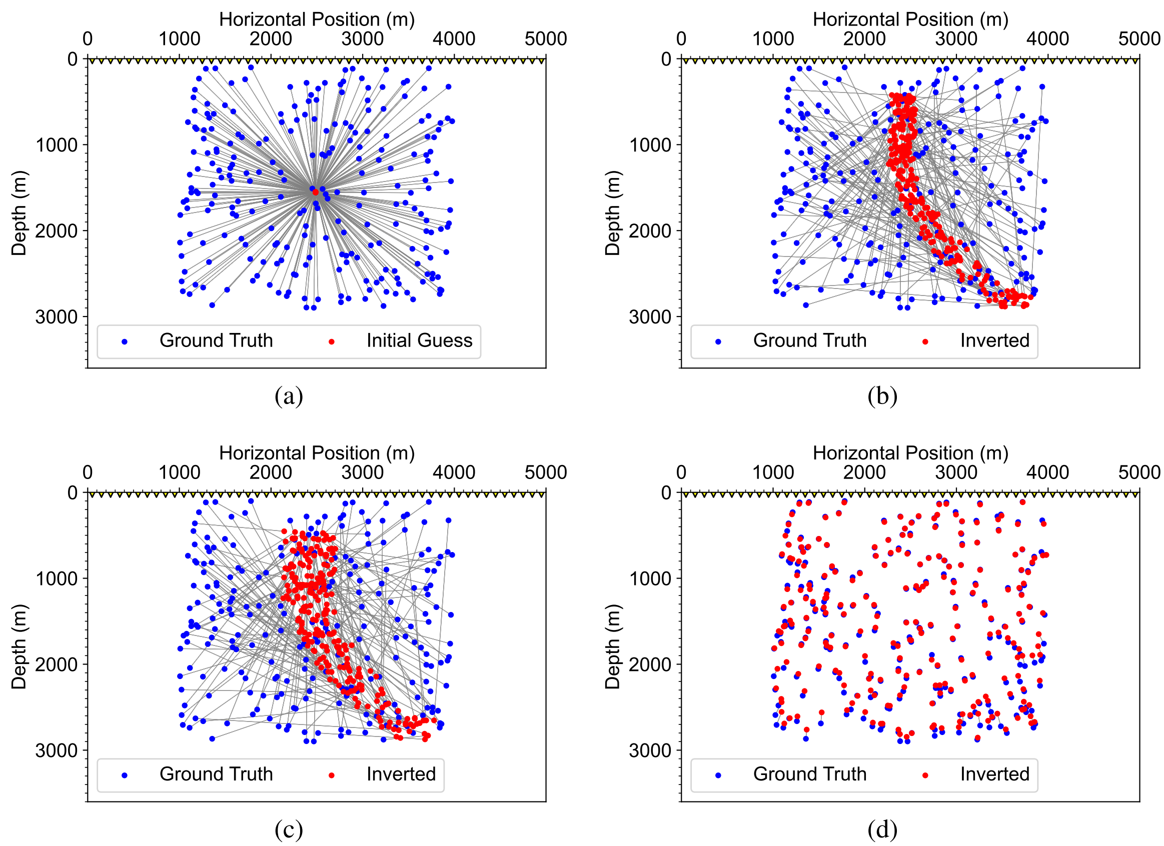

Figure 10: (a) Initial source locations and (b-d) inverted source locations in the 5th, 10th, and 100th iterations obtained using AD-TLOC, respectively.

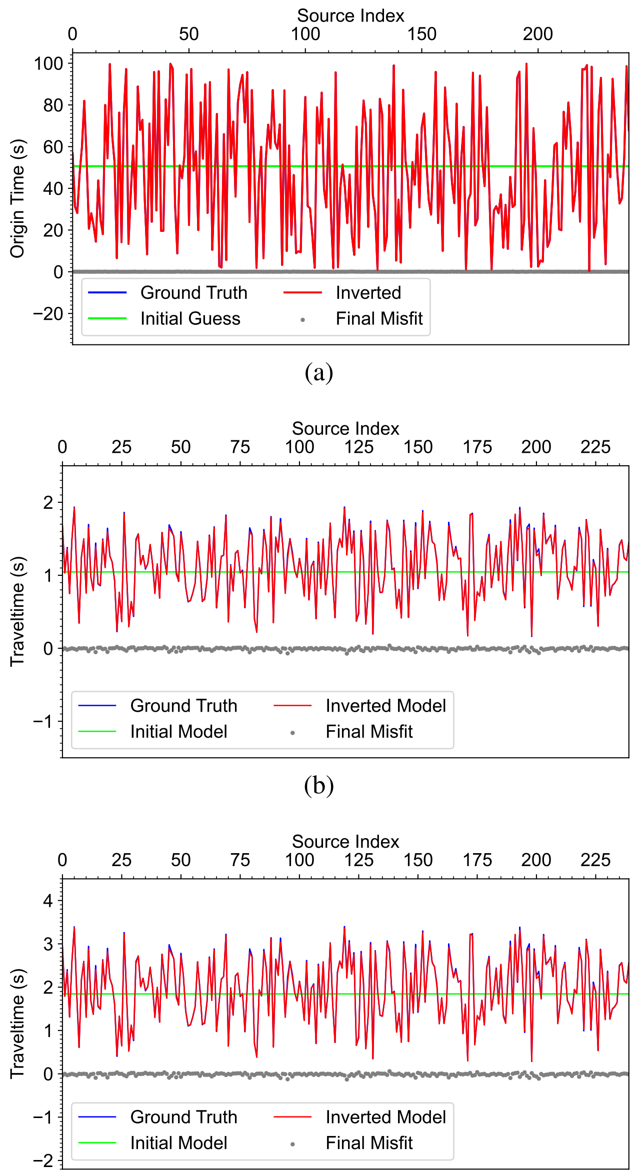

(a)

(b)

(c)

Figure 11: Comparisons among the ground-truth, initial guess, and synthetic values in the final inversion model regarding (a) the origin time, (b) P-arrival traveltime, and (c) S-arrival traveltime. The gray dots in the panels represent absolute differences between the synthetic and ground-truth values.

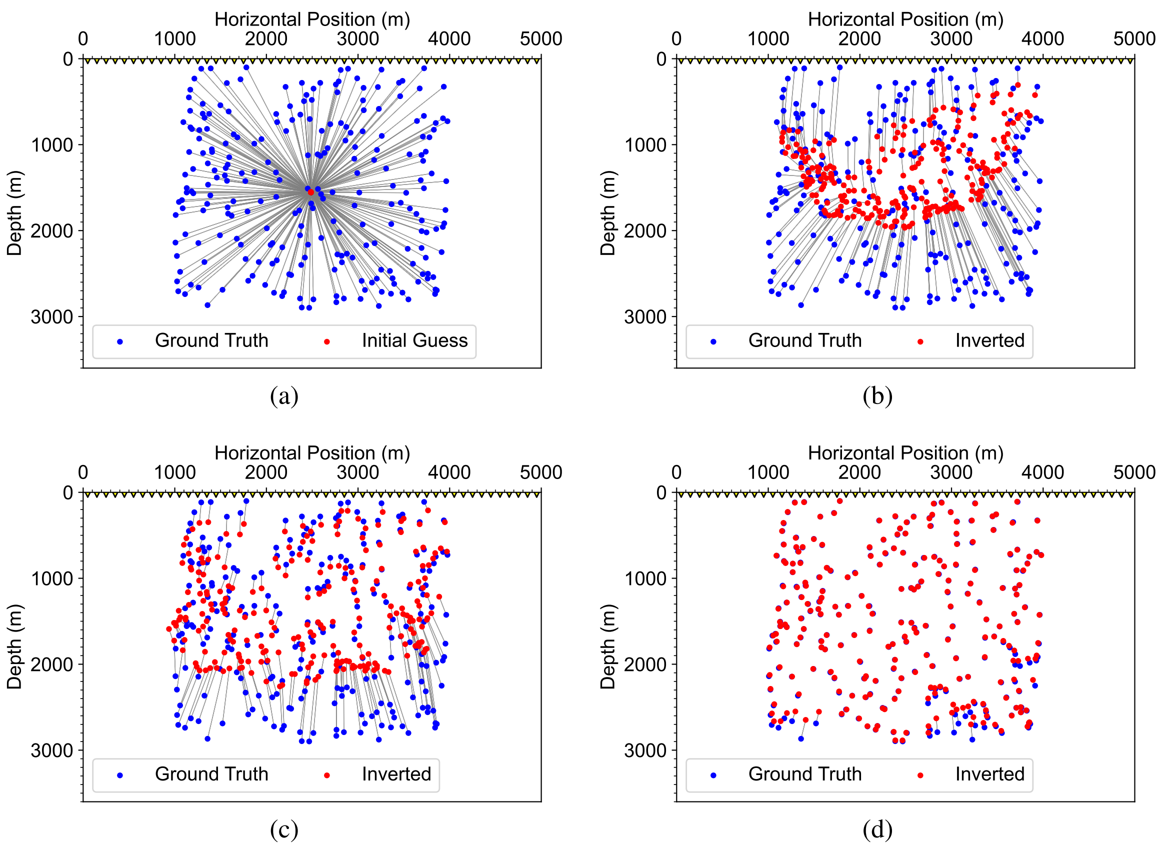

Figure 12: (a) Initial source locations and (b-d) inverted source locations in the 5th, 10th, and 100th iterations using DD-TLOC, respectively.

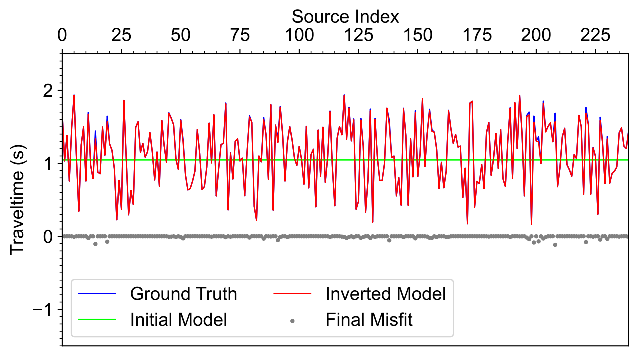

(a)

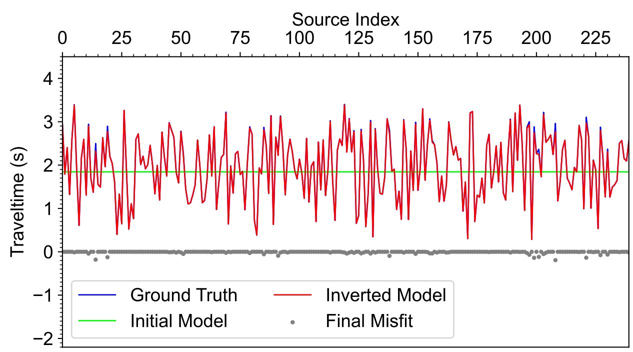

(b)

Figure 13: (a) Comparisons among the ground-truth traveltime $t_p - \eta_0$ (blue curve), the synthetic traveltime in the initial model $t_p^{(l=0)}$ (green curve), and the inverted model $t_p^{(l=100)}$ (red curve). Panel (b) displays the S-arrival traveltime result. The gray dots in the panels represent absolute differences between the synthetic and ground-truth values.

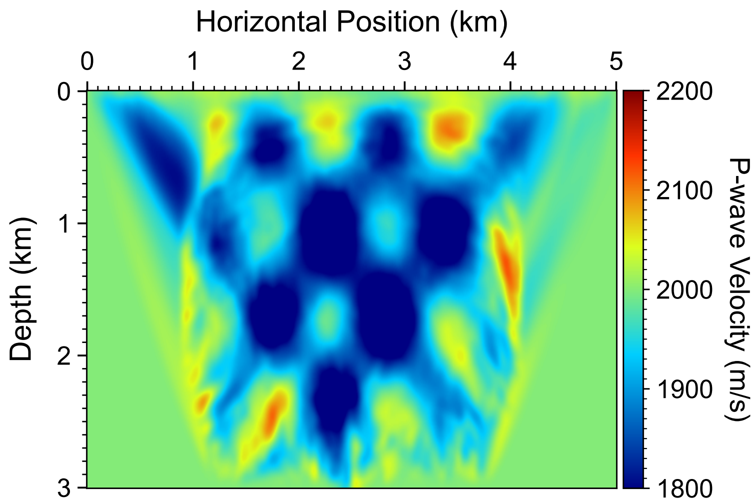

(a)

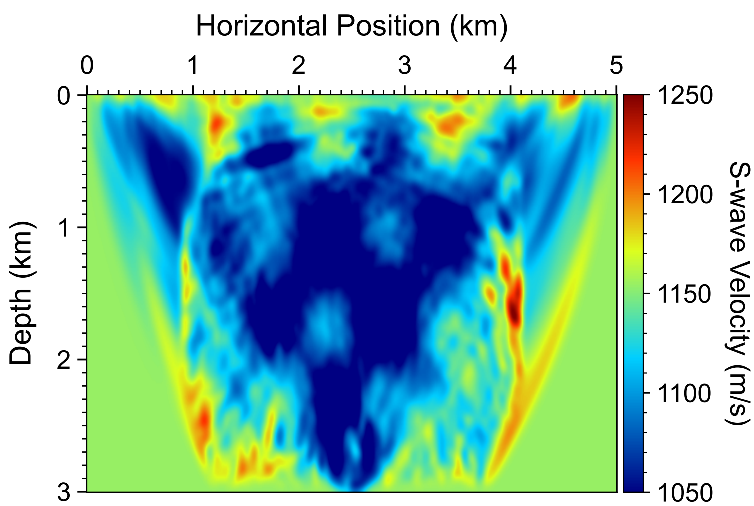

(b)

Figure 14: Inverted (a) v_p and (b) v_s models by DD-TLOC.

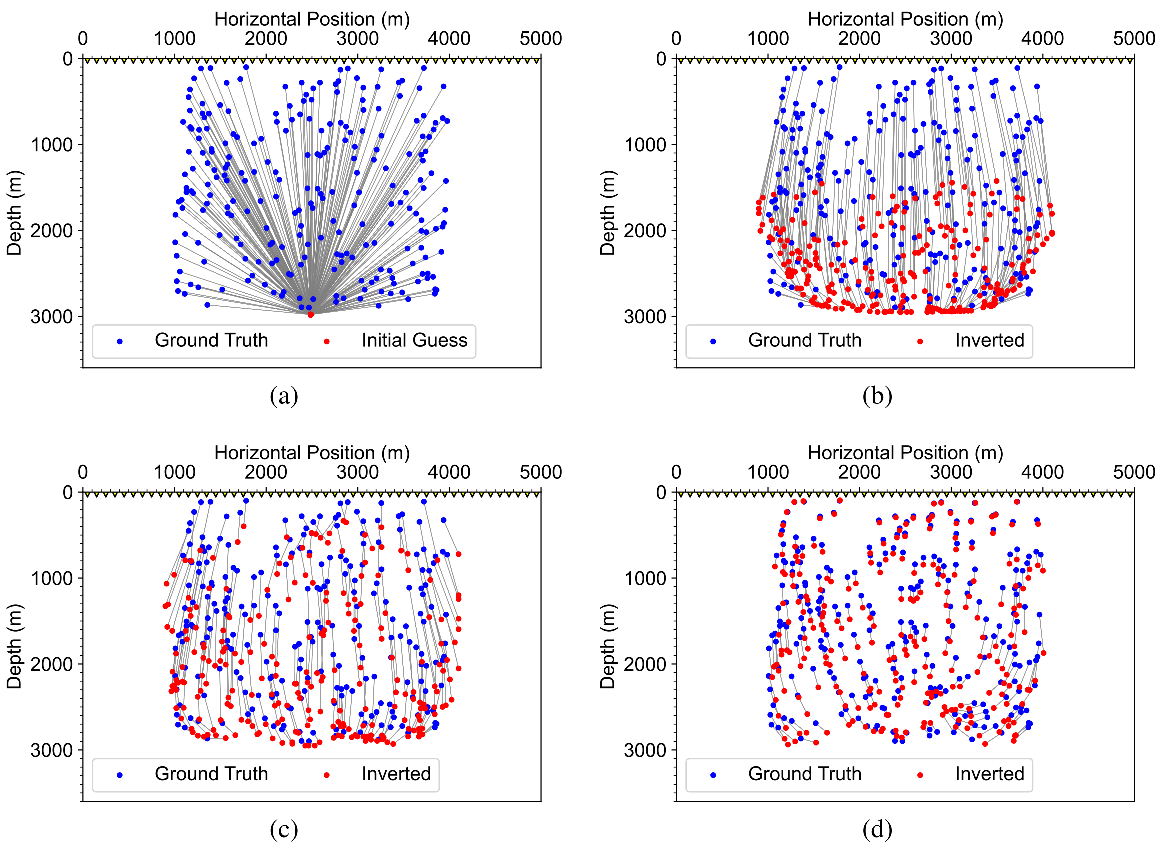

Figure 15: (a) Initial source locations and (b-d) inverted source locations in the 5th, 10th, and 100th iterations using DD-TLOC, respectively.

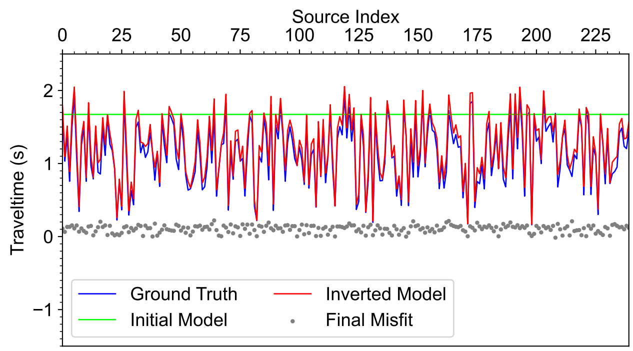

(a)

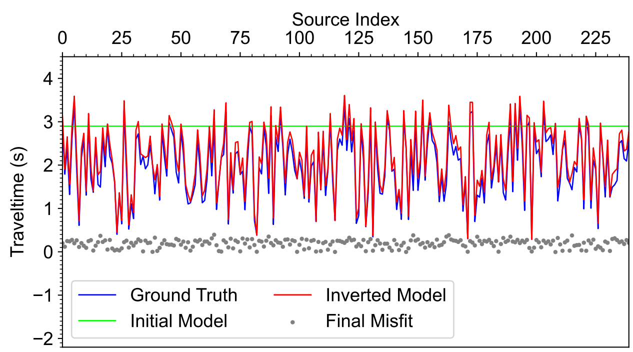

(b)

Figure 16: (a) Comparisons among the ground-truth traveltime $t_p - \eta_0$ (blue curve), the synthetic traveltime in the initial model $t_p^{(l=0)}$ (green curve), and the inverted model $t_p^{(l=100)}$ (red curve). Panel (b) displays the S-arrival traveltime result. The gray dots in the panels represent absolute differences between the synthetic and ground-truth values.

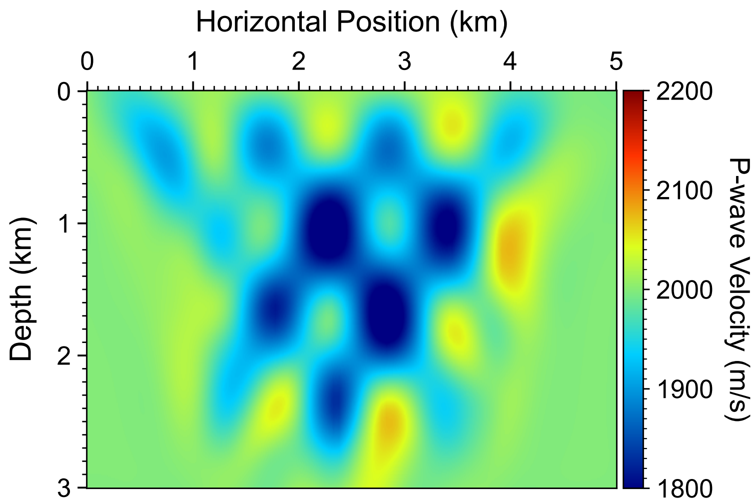

(a)

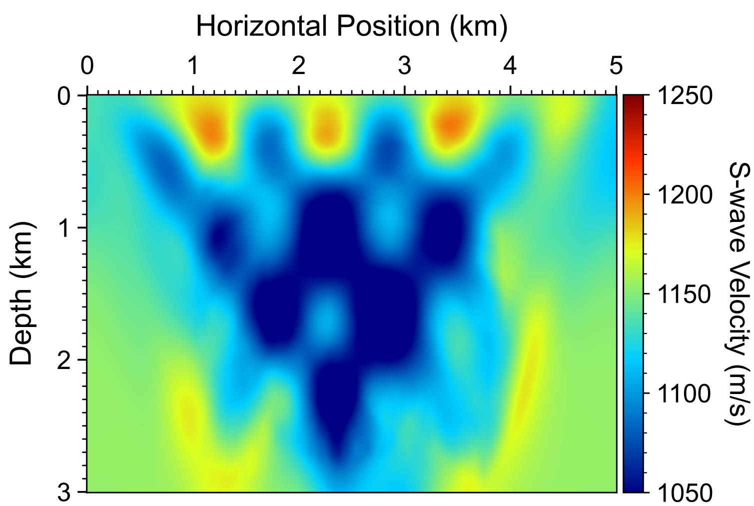

(b)

Figure 17: Inverted (a) v_p and (b) v_s models using regularized DD-TLOC.

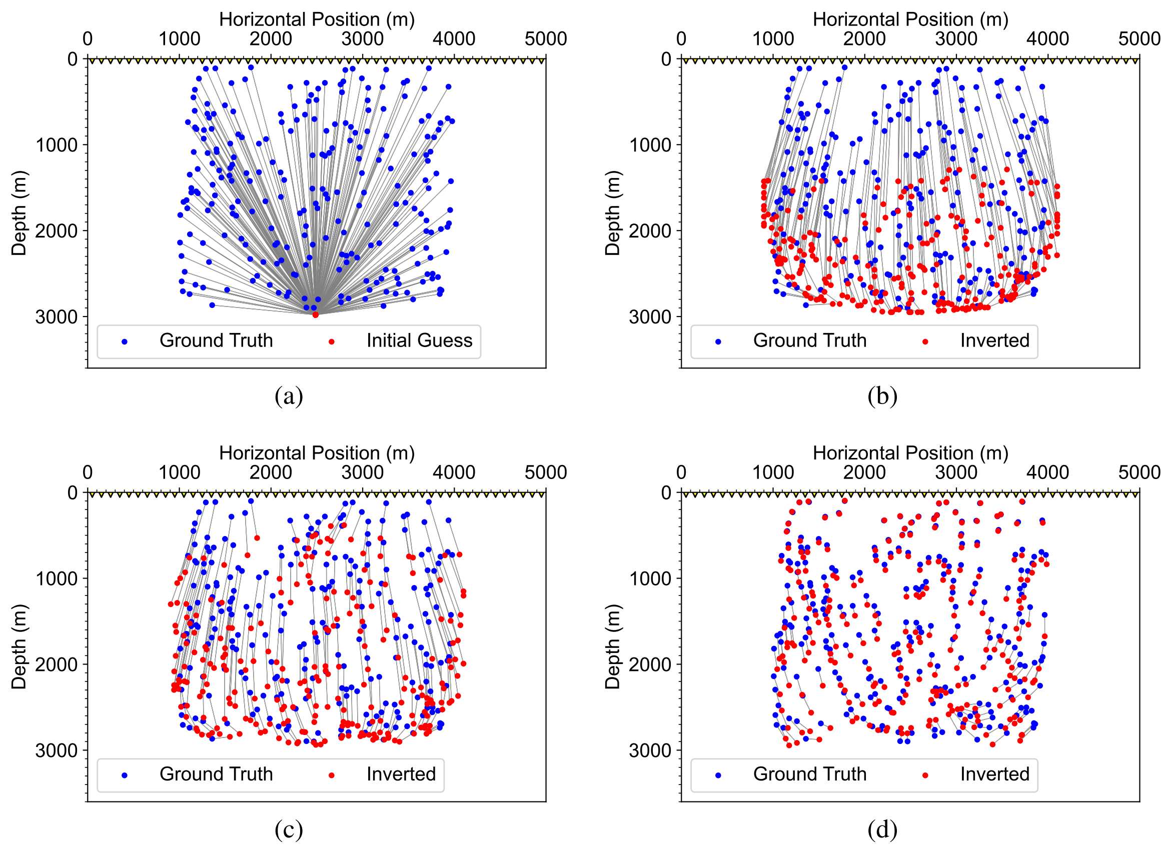

Figure 18: (a) Initial source locations and (b-d) inverted source locations in the 5th, 10th, and 100th iterations with regularized DD-TLOC, respectively.

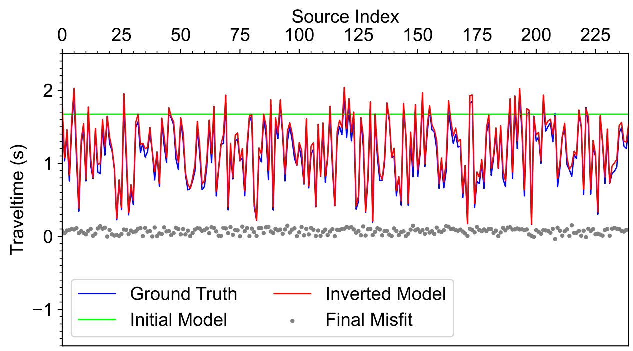

(a)

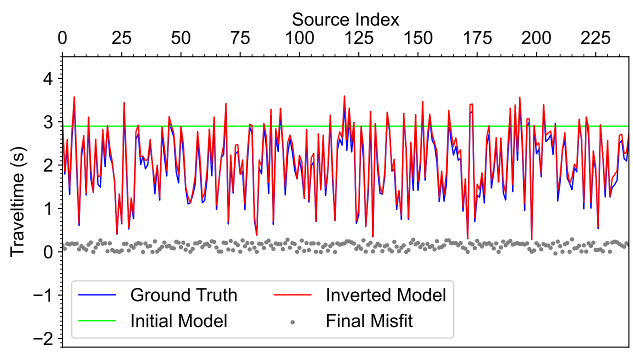

(b)

Figure 19: (a) Comparisons among the ground-truth traveltime $t_p - \eta_0$ (blue curve), the synthetic traveltime in the initial model $t_p^{(l=0)}$ (green curve), and the inverted model $t_p^{(l=100)}$ (red curve). Panel (b) displays the S-arrival traveltime result. The gray dots in the panels represent absolute differences between the synthetic and ground-truth values.

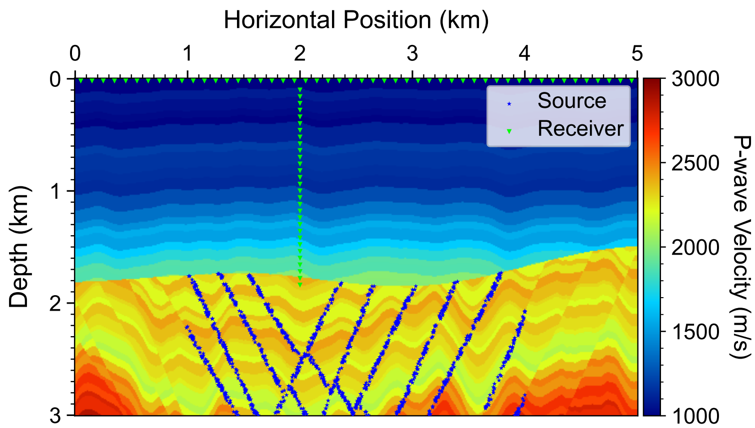

(a)

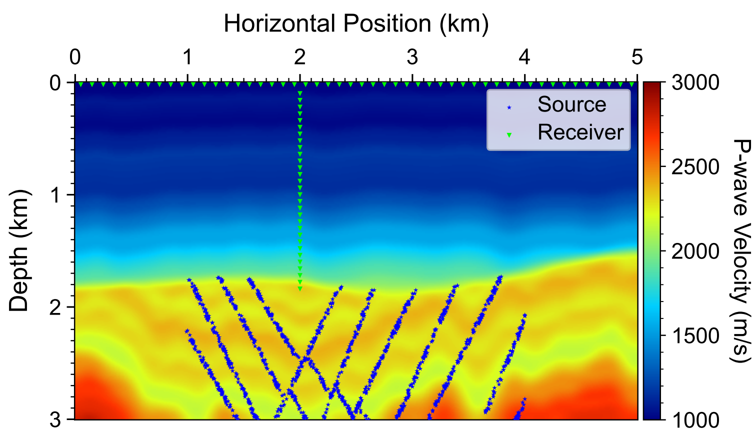

(b)

Figure 20: (a) A v_p model overlain by sources and receivers, and (b) a v_p model by smoothing the model in Panel (a) with a Gaussian filter for validating TLOC.

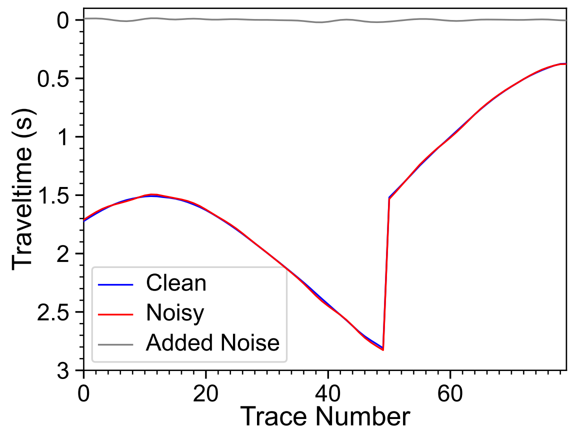

(a)

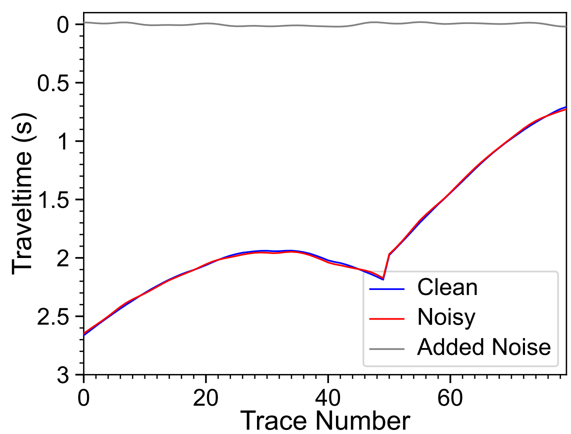

(b)

Figure 21: Two examples of clean and noisy data. For clarity, the origin time is subtracted from the data. In both panels, the noise data are generated by adding smoothed random noise displayed as a gray curve (consisting of 80 points) on the top. All the 1,200 common-source gathers are added with similar noise as in this figure to mimic time picking error in practice.

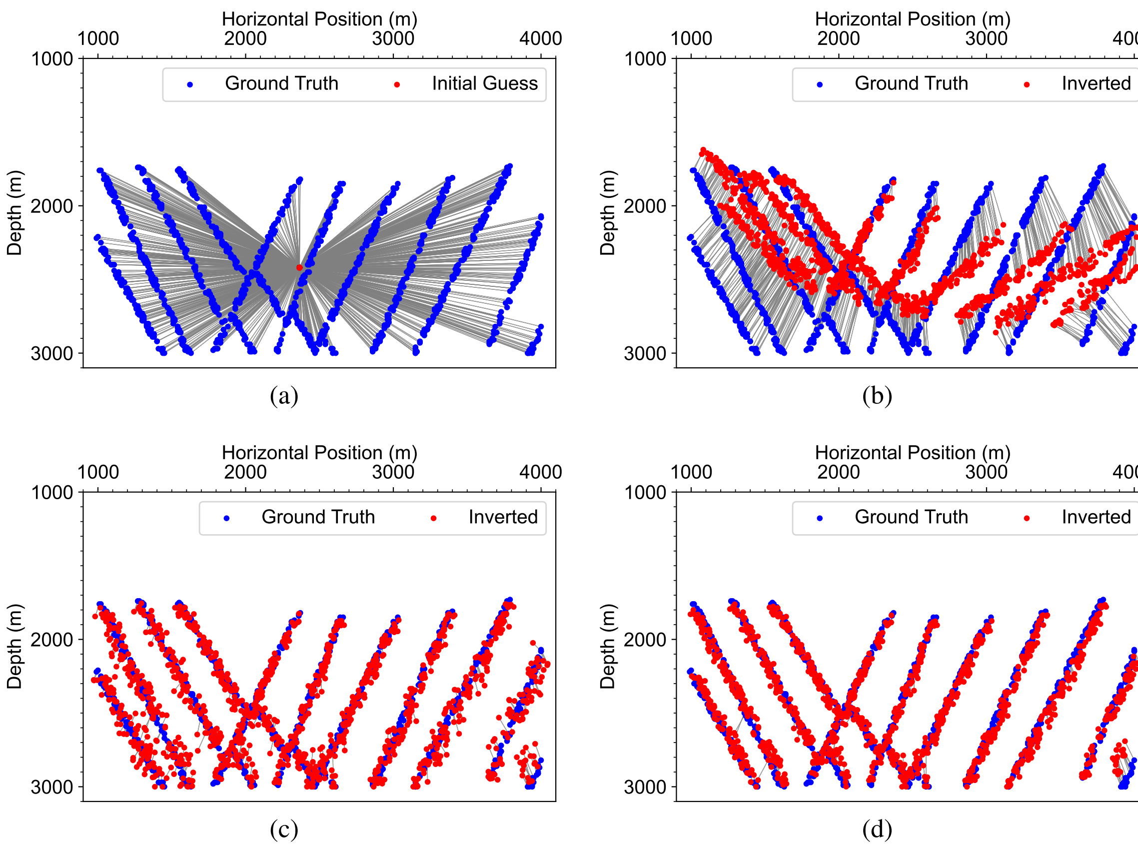

Figure 22: (a) Initial source locations, (b) inverted source locations using TLOC at the 5th iteration (for both cases of with and without ML-based source regularization), (c) inverted source locations using TLOC at the 50th iteration without ML-based source regularization, and (d) with ML-based source regularization.

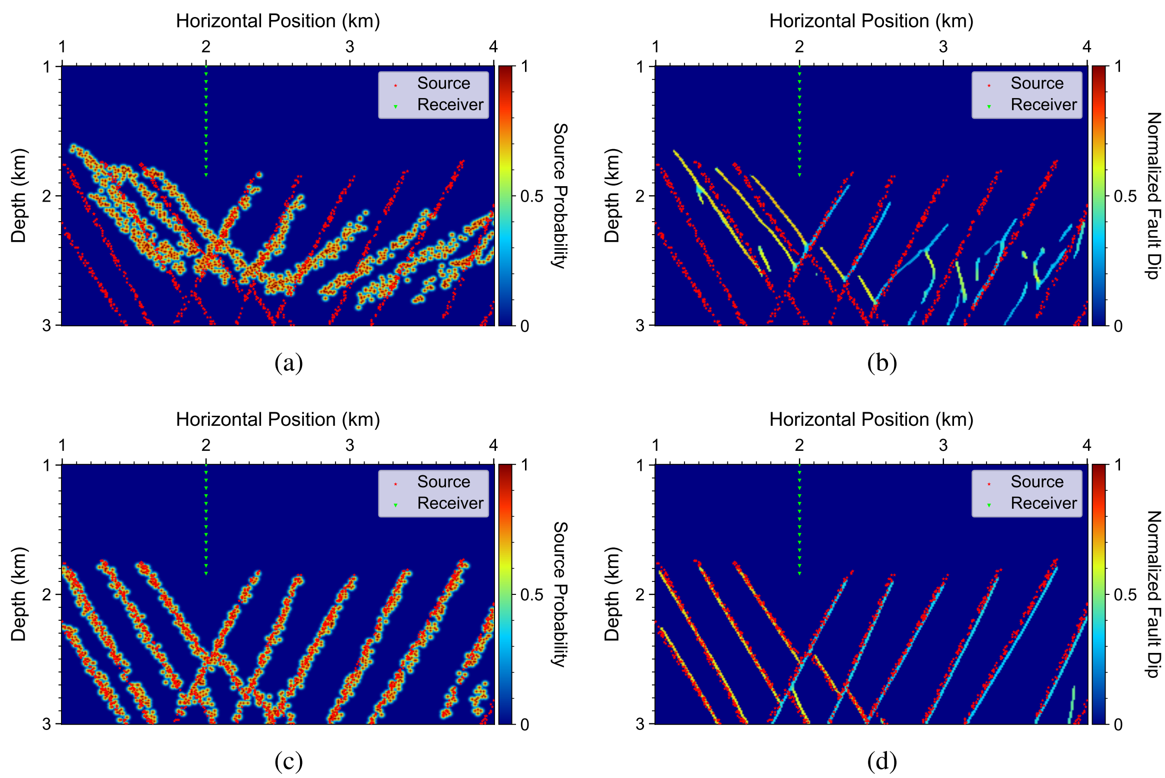

Figure 23: (a-b) Source image and ML-inferred and refined fault dip image in the 5th iteration, and (c-d) in the 50th iteration.

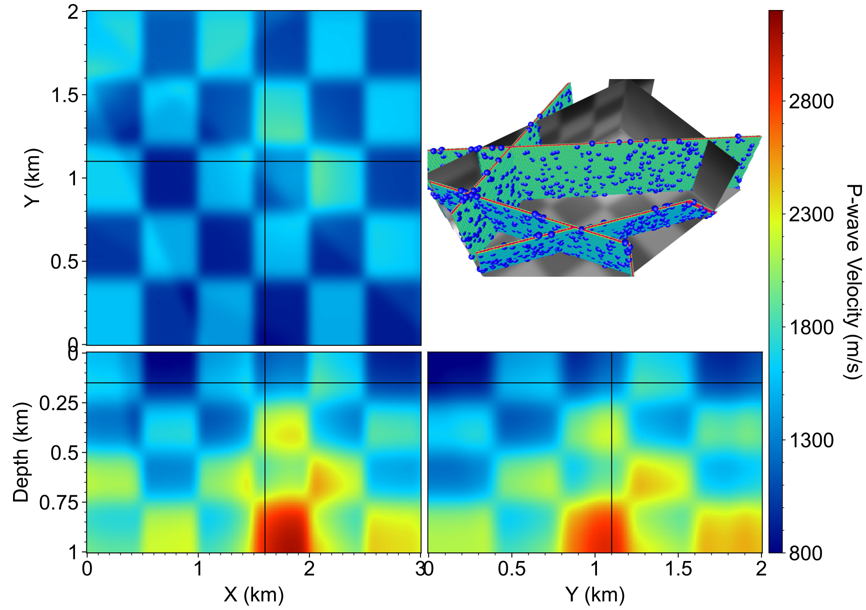

(a)

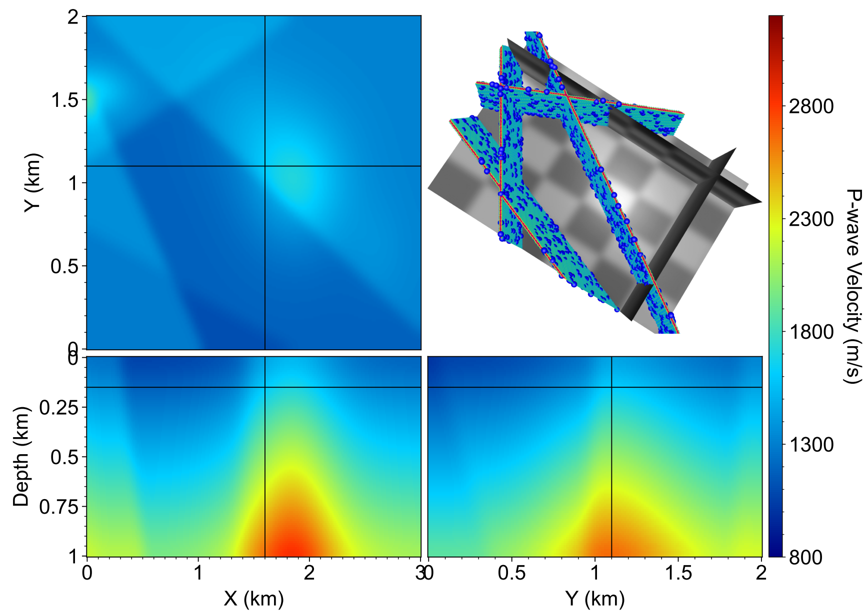

(b)

Figure 24: (a) A 3D heterogeneous v_p model with four intersecting faults designed for validating LATTE's DD-TLOC joint tomography-location. (b) The background smooth velocity model. The 3D plots at the top-right corner of both panels show the ground-truth fault surfaces and source locations.

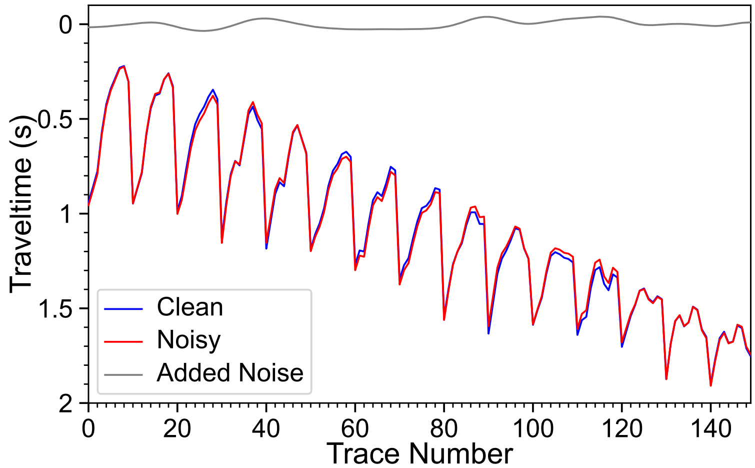

(a)

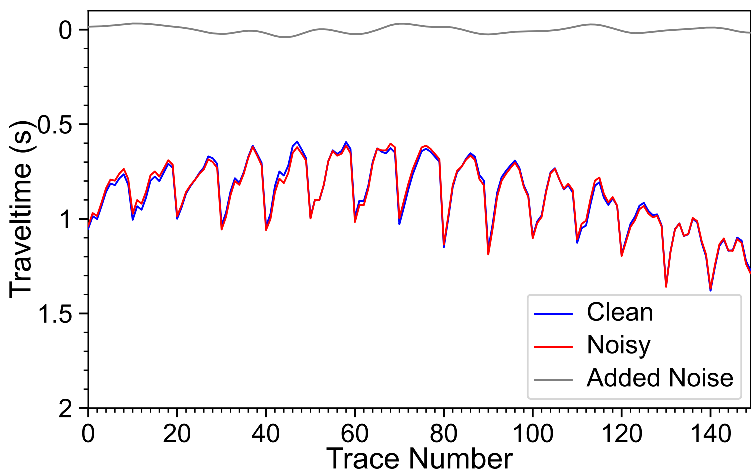

(b)

Figure 25: Two examples of clean and noisy data. For clarity, the origin time is subtracted from the data. In both panels, the noise data are generated by adding smoothed random noise displayed as a gray curve (consisting of 150 points) on the top. All the 1,200 common-source gathers are added with similar noise as in this figure to mimic time picking error in practice.

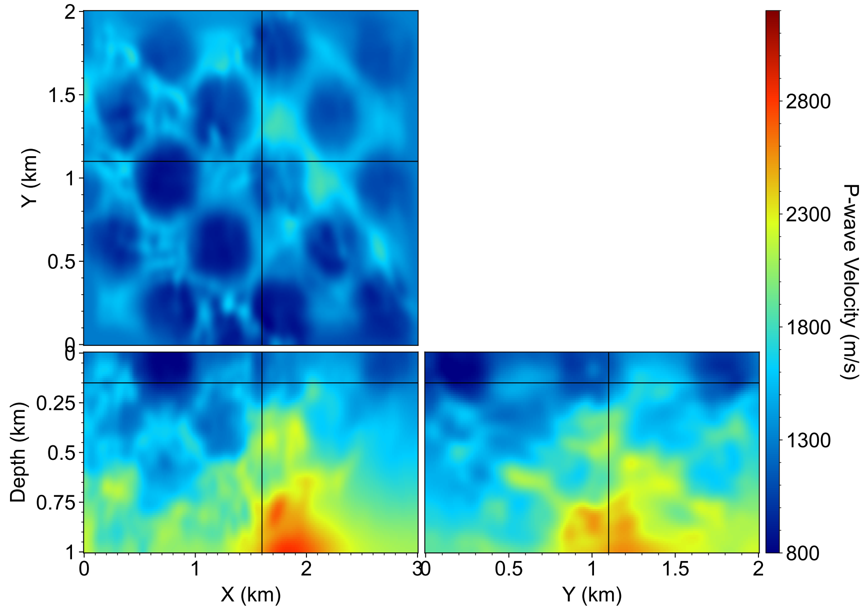

(a)

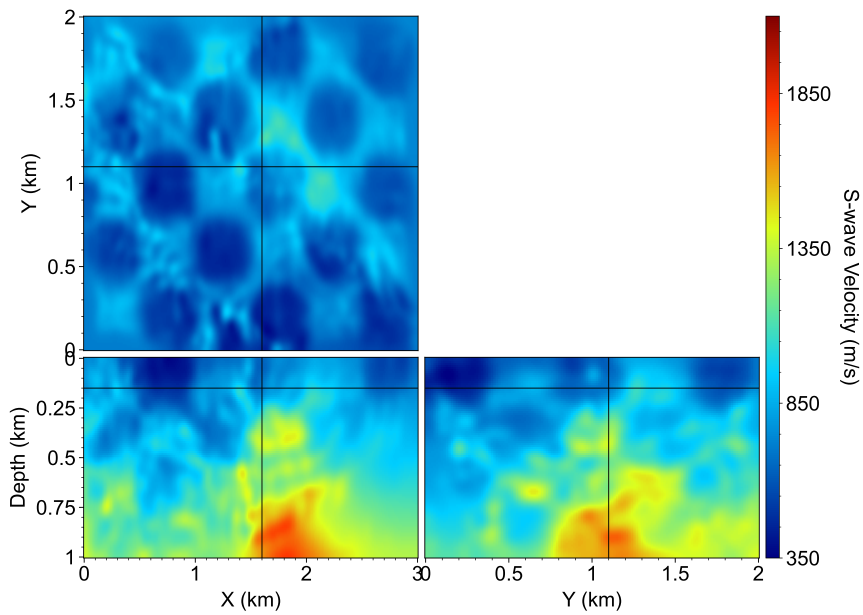

(b)

Figure 26: Inverted (a) v_p and (b) v_s models using DD-TLOC without model or source parameter regularization.

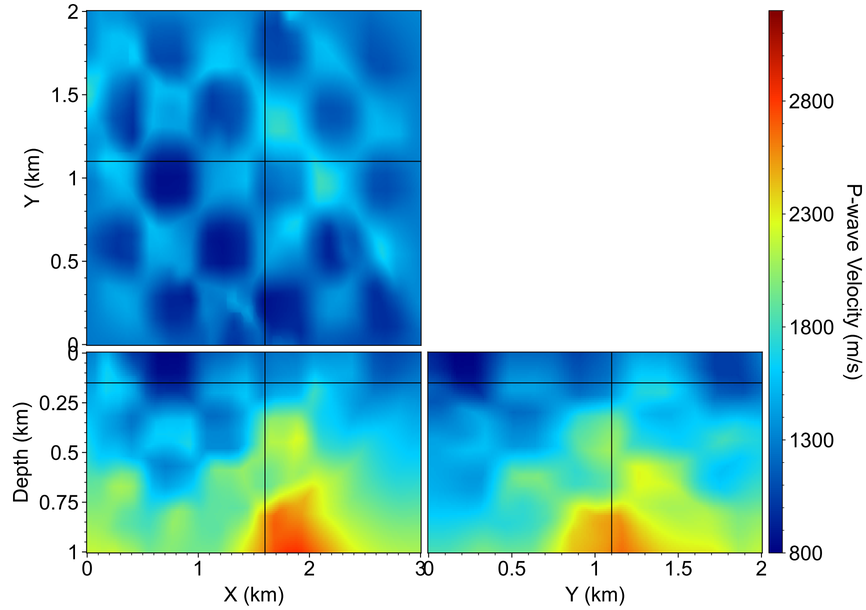

(a)

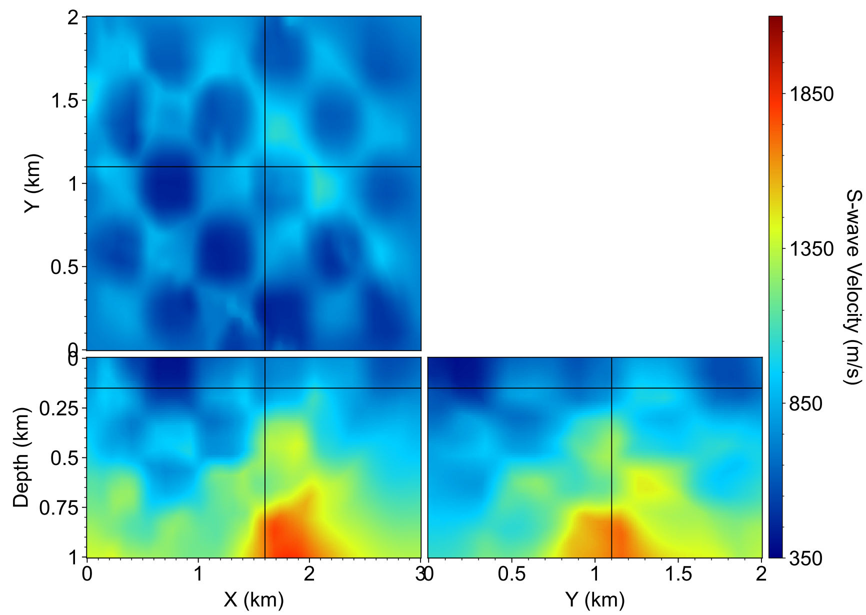

(b)

Figure 27: Inverted (a) v_p and (b) v_s models using DD-TLOC with model and source parameter regularization.

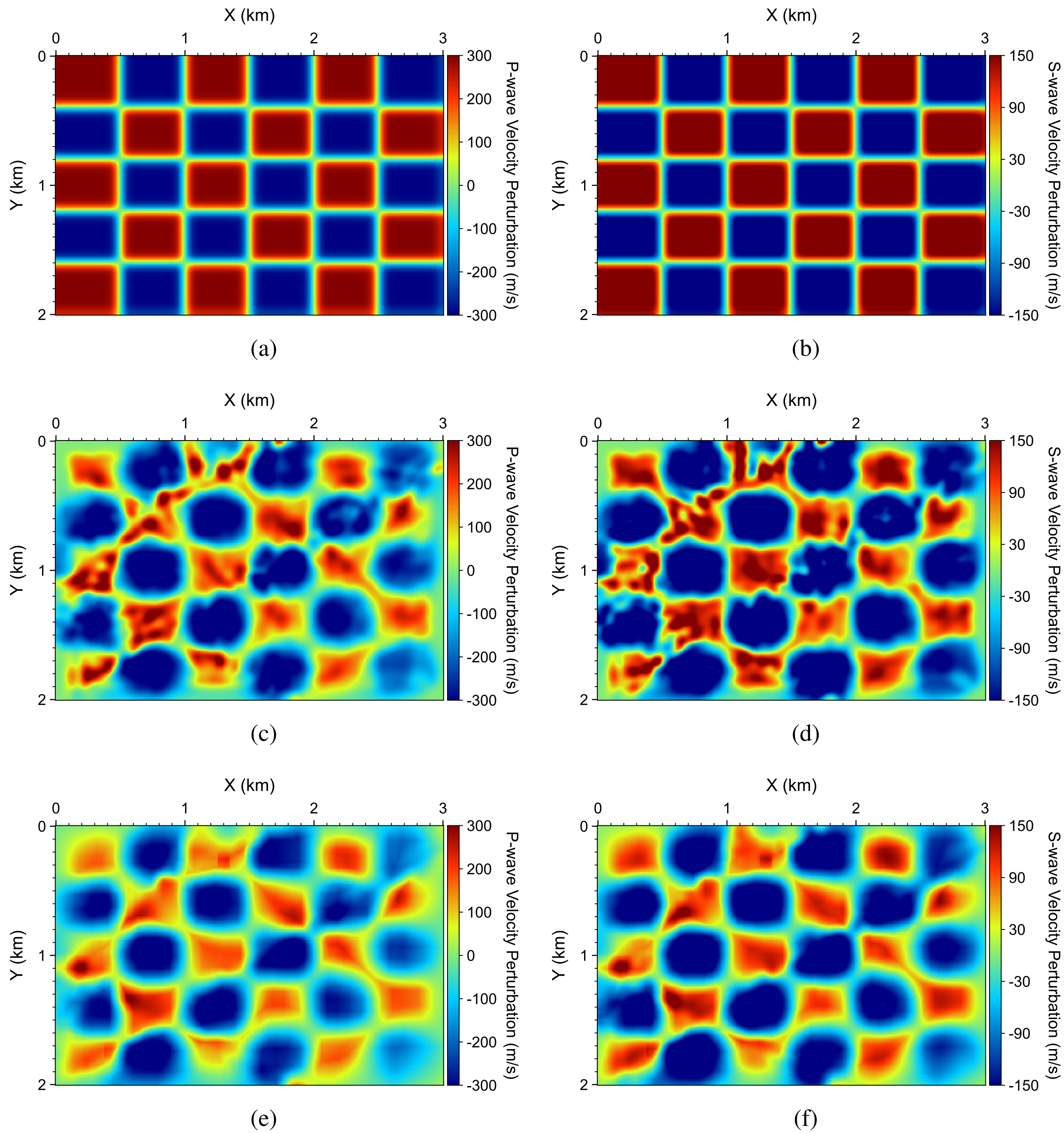

Figure 28: (a-b) Ground-truth Δv_p and Δv_s at a depth of 100 m, (c-d) inverted Δv_p and Δv_s by DD-TLOC without model parameter regularization, and (e-f) inverted Δv_p and Δv_s with model parameter regularization.

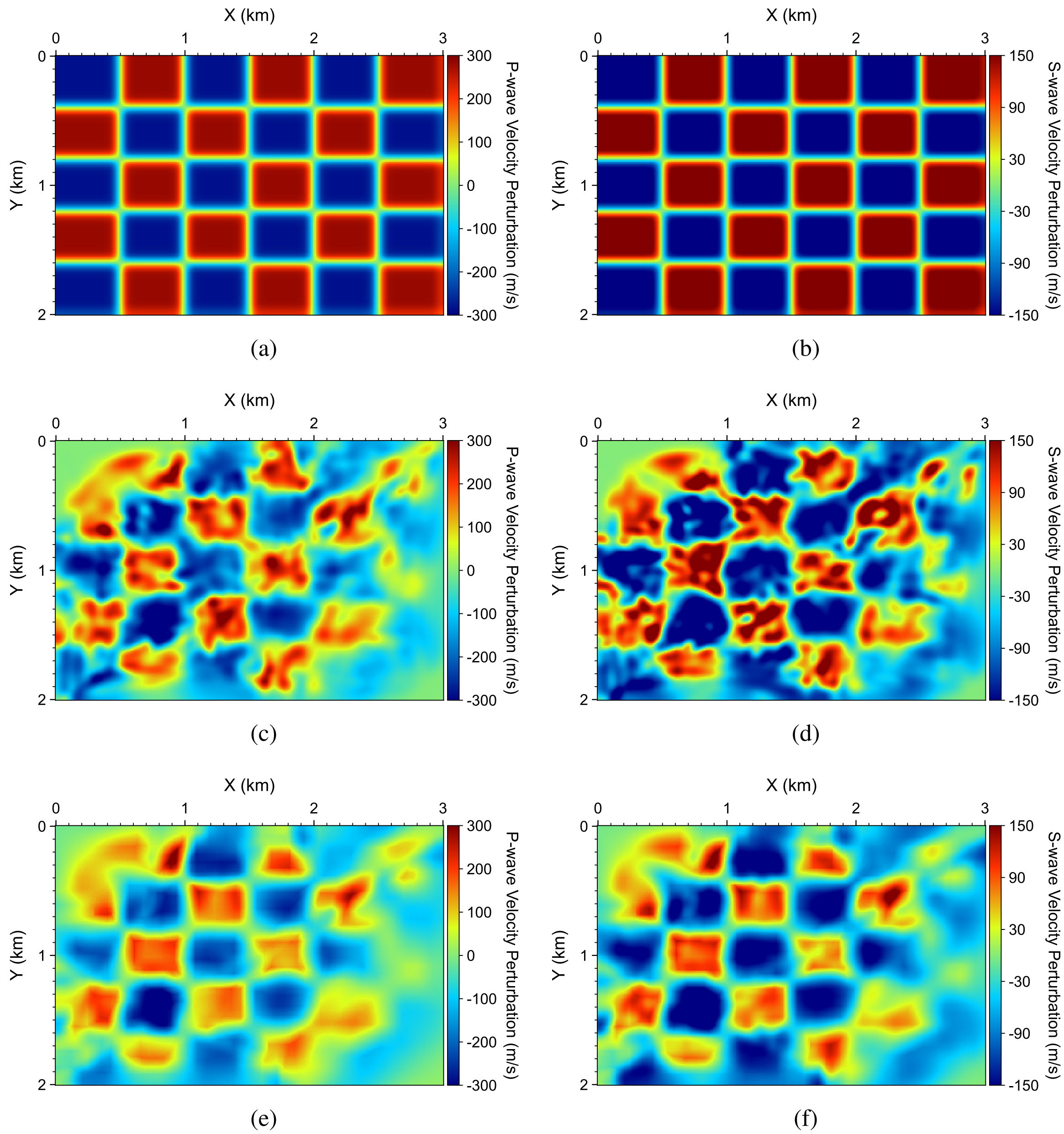

Figure 29: (a-b) Ground-truth Δv_p and Δv_s at a depth of 340 m, (c-d) inverted Δv_p and Δv_s by DD-TLOC without model parameter regularization, and (e-f) inverted Δv_p and Δv_s with model parameter regularization.

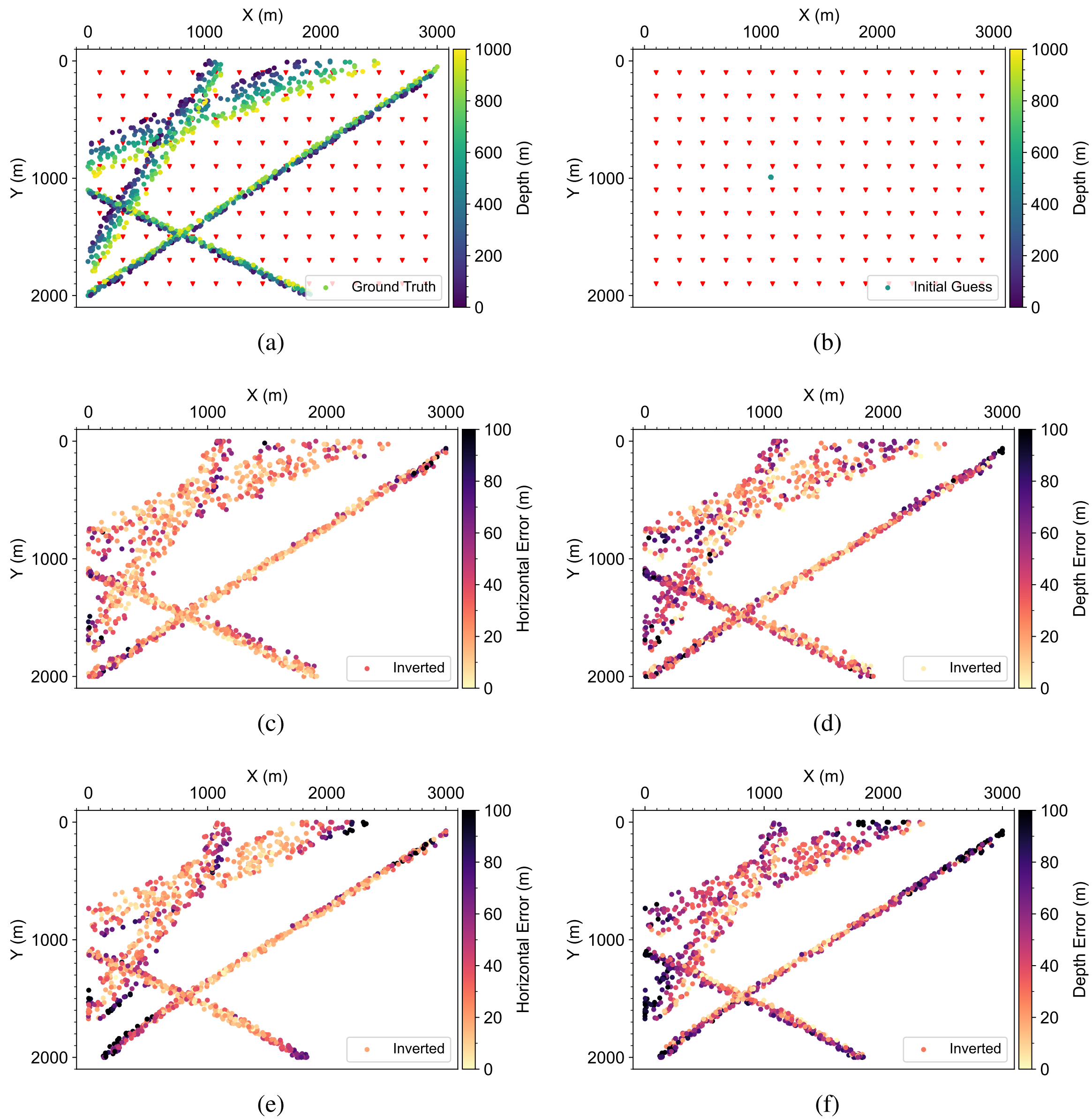

Figure 30: Map views of (a) ground-truth source locations colored by their depth, (b) initial source locations, (c-d) inverted source locations colored by horizontal/depth errors at the 50th iteration without ML-based source parameter regularization, and (e-f) inverted source locations colored by horizontal/depth errors with ML-based source parameter regularization.

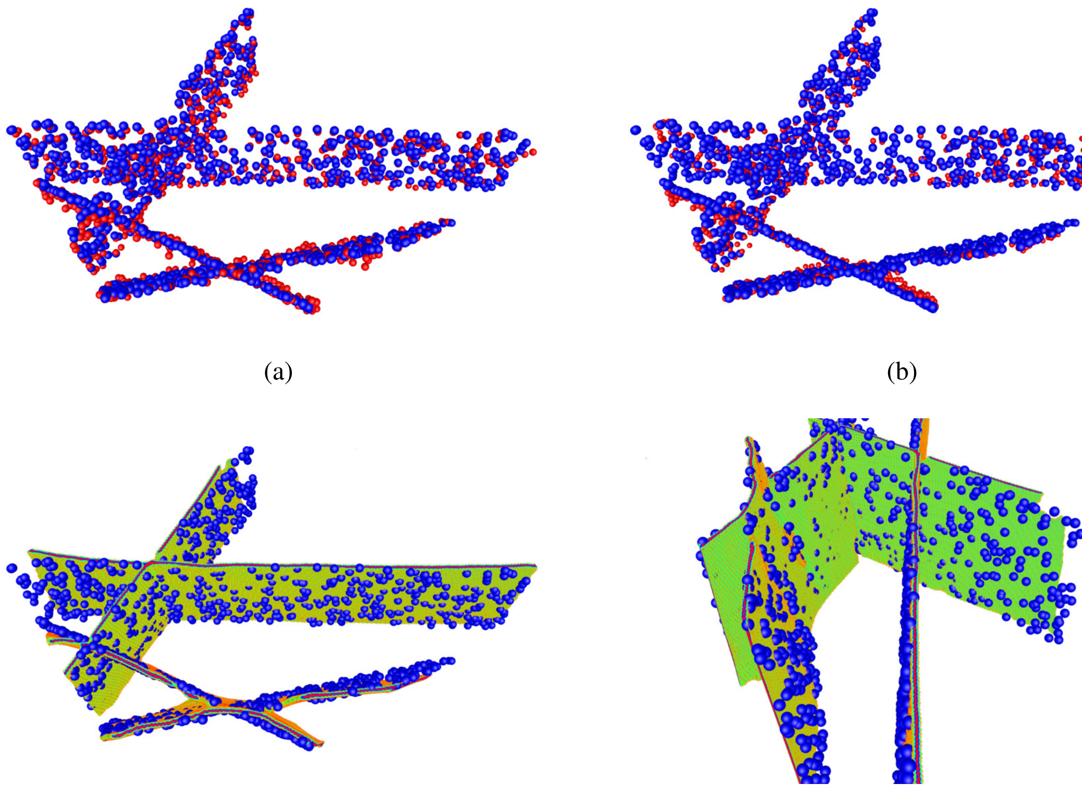

(a) (b) (c) (d)

Figure 31: (a) A comparison between ground-truth source locations (blue balls) and DD-TLOC-inverted source locations without source parameter regularization (red balls). (b) A similar comparison with that in Panel (a) but the red balls represent the source locations inverted by DD-TLOC with source parameter regularization. (c-d) 3D views of the ground-truth source locations (blue balls) and the faults inferred and refined using our multitask NNs in the 50th iteration.

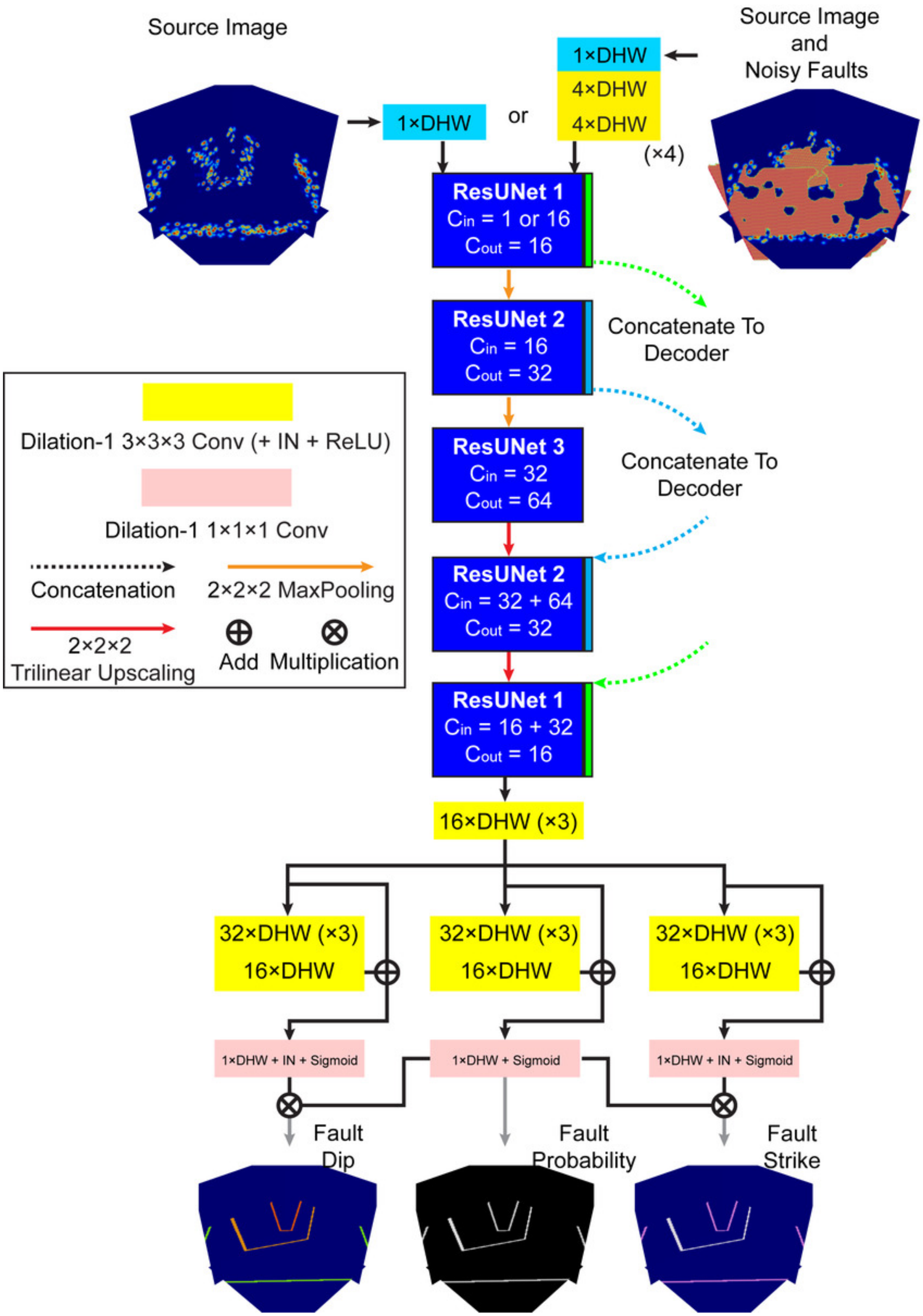

Figure 32: Architecture of our multitask fault inference and refinement NNs for inferring/refining fault attributes from a source image.